CHALMERS

Computational Aerodynamics and Aeroacoustics of Low-Pressure Axial Fans

DEBARSHEE GHOSH

Department of Mechanics and Maritime Sciences
CHALMERS UNIVERSITY OF TECHNOLOGY
Gothenburg, Sweden 2025

Thesis for the degree of Doctor of Philosophy

Computational Aerodynamics and Aeroacoustics of Low-Pressure Axial Fans

Debarshee Ghosh

Department of Mechanics and Maritime Sciences
CHALMERS UNIVERSITY OF TECHNOLOGY
Göteborg, Sweden 2025

Computational Aerodynamics and Aeroacoustics of Low-Pressure Axial Fans
Debarshee Ghosh
ISBN 978-91-8103-169-0

Doktorsavhandlingar vid Chalmers tekniska högskola
Ny serie nr 5627
ISSN 0346-718X

Department of Mechanics and Maritime Sciences
Chalmers University of Technology
SE–412 96 Göteborg, Sweden
Telephone + 46 (0) 31 – 772 1000

Chalmers Reproservice
Göteborg, Sweden 2025

To Nikita and my family ..

Abstract

Computational Aerodynamics and Aeroacoustics of Low-Pressure Axial Fans
DEBARSHEE GHOSH
Division of Fluid Dynamics
Chalmers University of Technology

Electric cooling-fans, or E-fans, play a crucial role in automotive thermal management systems. These fans are typically low-pressure axial fans powered by electric motors. In electric vehicles, cooling-fans generate airflow to reject heat from the coolant circulating through the heat exchanger. These fans are typically operational at low vehicle speeds.

Due to increasingly compact underhood spaces, manufacturers seek greater flexibility in fan placement. As a result, cooling-fans are often placed downstream of other underhood components and consequently ingest spatially non-uniform and turbulent flow. Additionally, to achieve greater flexibility in the placement of cooling-fans, multiple small-diameter fans are often arranged in parallel instead of using a single large-diameter fan. Furthermore, in electric vehicles, the absence of masking noise from the internal combustion engine makes the noise produced by cooling-fans more significant.

Both rotor blade geometry and inflow conditions—which depend on fan installation—influence turbomachines' aerodynamic performance and noise. This work examines the effects of rotor blade design and installation on the aerodynamic and aeroacoustic performance of low-pressure axial fans using Computational Fluid Dynamics (CFD) and Computational Aeroacoustics (CAA).

Four rotor blade designs with varying blade-loading-distributions are generated using the Blade Element Momentum (BEM) method for low-solidity blades. Their aerodynamic performance is evaluated under both uniform and non-uniform inlet flow conditions, using a generic non-uniform profile. The aeroacoustic performance is evaluated numerically only under uniform inflow conditions.

Installation effects are studied through four numerical investigations, analyzing the aerodynamic and aeroacoustic impacts of an upstream blockage, parallel operation of two low-pressure axial fans, and reduced inlet bellmouth dimensions. Ultimately, this study summarizes the design process for low-pressure axial fans and typical installation effects.

Keywords: cooling-fans, low-pressure axial fans, upstream blockage, fans in parallel, blade design, CFD, CAA

Acknowledgments

This research was performed at the Division of Fluid Dynamics at Chalmers University of Technology from July 2020 to March 2025. I would like to thank all the collaborators of this project; Chalmers University of Technology, Volvo Group Technology, Volvo Car Corporation, and the Swedish Energy Agency, without whom this work would be impossible.

I would like to express my deepest gratitude to Professor Niklas Andersson and Associate Professor Sassan Etemad for selecting me to participate in this project and granting me the opportunity to pursue my Ph.D. To Professor Niklas Andersson, I am especially thankful for always taking the time to listen to me, being my sounding board, and teaching me to trust the process. I am sure being my sounding board was an especially difficult task, as you were at the receiving end of some truly horrendous ideas. Words cannot fully express my gratitude for having had you as my supervisor. Any success I may achieve in my future career will, in no small part, be a reflection of the time spent working with you.

To Associate Professor Sassan Etemad, I am deeply grateful for your patience and unwavering belief in me. You gave me the freedom to chart my own course through the Ph.D., even when it occasionally diverged from the project's original goals, which I deeply appreciate. Your support allowed me to grow both as a researcher and as an individual.

I would like to express my deepest gratitude and love to my family for their unwavering support and patience, and without whom none of my achievements would have been possible. Most of all, I would like to thank my dear wife, Nikita, for her unwavering support in everything I did. I imagine I haven't made it easy, with my mood often fluctuating according to my residuals. But you've been my most reliable 'under-relaxation factor,' consistently ensuring I didn't diverge.

I would like to thank all my colleagues at the Division of Fluid Dynamics for creating a pleasant working environment over the past five years. A special shout-out to Marily, Oliver, Martina, and Vinicius. As an international Ph.D. student, life can often be lonely, and all of you ensured I didn't miss home too much, and for listening to the million complains I had on a daily basis. A huge thank you to Gonzalo and Sudharsan as well for making the start of my Ph.D.— during a global pandemic — bearable.

Debarshee Ghosh
Göteborg, February 2025

List of Publications

This thesis is based on the following appended papers:

Paper 1: Ghosh, D., Andersson, N., and Etemad, S., "Computational Fluid Dynamics Simulations of Aerodynamic Performance of Low-Pressure Axial Fans with Upstream Blockage," SAE Technical Paper 2024-01-2409, 2024, https://doi.org/10.4271/2024-01-2409.

Paper 2: Ghosh, D., Andersson, N., and Etemad, S. (January 24, 2024). "Aerodynamic Analysis of Low-Pressure Axial Fans Installed in Parallel." ASME. J. Fluids Eng. May 2024; 146(5): 051204. https://doi.org/10.1115/1.4064292

Paper 3: Ghosh, D., Vourakis, M., Andersson, N., and Etemad, S. (October 23, 2024). "Computational Aeroacoustics of Low-Pressure Axial Fans Installed in Parallel." ASME. J. Fluids Eng. February 2025; 147(2): 021204. https://doi.org/10.1115/1.4066752

Paper 4: Ghosh, D., Andersson, N., and Etemad, S., "Computational Aeroacoustics of Inlet Geometry on Tip Noise for Low Pressure Axial Fans," AIAA SCITECH 2025 Forum, https://doi.org/10.2514/6.2025-2166.

Paper 5: Ghosh, D., Vourakis, M., Boström, A., Andersson, N., Roy, A., Etemad, S., "Evaluation of hybrid computational aeroacoustic methods applied to automotive cooling-fans", Fan 2025 Conference

Paper 6: Ghosh, D., Andersson, N., and Etemad, S., "Aerodynamic and Aeroacoustic Effect of Blade Loading Distribution For Low-Pressure Axial Fans"

Nomenclature

Acronyms

ADP	–	Aerodynamic Design Point
BEM	–	Blade Element Momentum
BEP	–	Best Efficiency Point
BL	–	Boundary Layer
BPF	–	Blade Passing Frequency
CAA	–	Computational Aeroacoustics
CFD	–	Computational Fluid Dynamics
DDES	–	Delayed Detached Eddy Simulation
FAU	–	Friedrich Alexander University
FWH	–	Ffowcs-Williams and Hawkings
HVAC	–	Heating Ventilation and Air Conditioning
ICE	–	Internal Combustion Engine
IEA	–	International Energy Agency
LE	–	Leading Edge
NACA	–	National Advisory Committee for Aeronautics
RANS	–	Reynolds-Averaged Navier Stokes
SPL	–	Sound Pressure Level
SWL	–	Sound Power Level
TE	–	Trailing Edge
URANS	–	Unsteady Reynolds-Averaged Navier Stokes

Latin Letters

C_D	–	drag coefficient
C_L	–	lift coefficient
F_c	–	centrifugal force
H	–	convective heat transfer rate
L	–	eddy diameter
L_p	–	sound pressure level
L_w	–	sound power level
P_B	–	blade power
P_{shaft}	–	input shaft power

Q – volume flowrate
T – temperature
T_{shaft} – input shaft torque
U – blade velocity
U_c – eddy convection velocity
Y – specific work
Y_B – specific blade energy
$\dot{m}$ – mass flowrate
a – blade loading constant for radius dependent blade loading distribution
b – blade loading constant for linear, polynomial and parabolic design
c – velocity in absolute frame of reference
c_o – speed of sound
c_p – specific heat capacity
d – blade loading constant for parabolic design
d_{fan} – fan diameter
d_{hub} – fan hub diameter
f – maximum camber of NACA airfoil
f – frequency
f_{BPF} – blade passing frequency
f_{SF} – shaft rotational frequency
k – turbulent kinetic energy
k – blade loading integration constant
l_c – chord length
m – blade loading constant for polynomial design
n – rotational speed in rps
n – number of elemental-blade-cascades along rotor blade span
p – pressure
$p^{'}$ – time varying pressure perturbation
r – blade radius
s_b – blade spacing
s_{tip} – fan tip gap
w – velocity in relative frame of reference
z_b – blade count

Greek Symbols

α – absolute flow angle
α – angle of attack
β – relative flow angle
γ – stagger angle
δ – specific diameter
δA – elemental area
δm – elemental mass

δQ	–	elemental volume flowrate
δr	–	elemental radius
ε	–	turbulence dissipation
ε	–	drag-to-lift ratio
η	–	aerodynamic efficiency
η_h	–	hydraulic efficiency
η_{vol}	–	volumetric efficiency
κ	–	hub-to-tip diameter ratio
λ	–	wavelength
Λ	–	integral turbulent length scale
ν	–	kinematic viscosity
ξ	–	pressure loss coefficient
ρ	–	fluid density
σ	–	specific speed
σ	–	blade solidity
φ	–	flow coefficient
ψ	–	pressure coefficient
ω	–	rotational speed
ω	–	turbulence frequency

Subscripts

θ	–	tangential component of velocity
B	–	blade
∞	–	fluid property in ambient condition
ax	–	axial component of velocity
ca	–	elemental blade cascade
d	–	dynamic component of pressure
hub	–	fluid property at rotor hub
m	–	meridional component of velocity
max	–	maximum
opt	–	optimum
rad	–	radial component of velocity
ref	–	reference
rms	–	root mean square
tip	–	fluid property at rotor tip
ts	–	total-to-static fluid property
tt	–	total-to-total fluid property
1	–	rotor inlet station
2	–	rotor outlet station
st	–	static fluid property
t	–	total fluid property

Non Dimensional Number

Ma – Mach number
Re – Reynolds number

Contents

Part I

Introductory Chapters

Chapter 1

Introduction

1.1 Background

As of 2022, transportation activities, i.e., road, rail, water, and air transport, accounted for 31% of the European Union's total greenhouse gas emissions [1]. Road transport alone accounted for 71% of the emissions associated with transportation activities [1].

Over the past decade, the automotive industry, has made significant efforts to reduce its global carbon footprint in compliance with the Paris Climate Agreement [2], by embracing electric mobility as the future of road-transport. Several automotive manufacturers are rapidly transitioning toward electric propulsion through battery electric vehicles, hybrid electric vehicles, plug-in hybrid electric vehicles and fuel cell electric vehicles. In general, an electric vehicle offers several advantages over its internal combustion engine (ICE) powered counterparts, including delivery of instant maximum torque, reduced cabin noise, lower maintenance, and reduced environmental impact [3].

The number of on-road electric vehicles is expected to grow steadily, driven by increasing customer acceptance, advancements in battery technology, and the expansion of battery-charging infrastructure. The International Energy Agency (IEA) estimated approximately 16.5 million on-road electric vehicles in 2021, and has predicted this number to increase rapidly to approximately 125 million by 2030 [4, 5]. However, as of 2021, electric vehicles accounted for less than 5% of the global vehicle fleet [4].

A key barrier to widespread customer adoption has been the lower autonomy of electric vehicles compared to ICE powered vehicles, i.e., shorter driving range and longer charging times. As of 2021, IEA estimated the median driving range of electric vehicles to be about half of the median range of ICE powered vehicles.

Increasing the driving range of electric vehicles typically requires larger batteries with higher storage capacity and energy density [6]. Since batteries produce electrical power through exothermic chemical reactions [7], increasing the energy density and storage capacity of battery packs leads to a corresponding increase in its thermal output.

The current generation of electric vehicles are typically powered by Lithium-ion battery packs. Lithium-ion is the preferred choice of cell chemistry due to its high specific energy, high energy density, long life cycle, and minimal memory effects [8, 9]. Multiple lithium-ion cells are combined to form a battery pack. In the absence of the ICE, the battery pack acts as the primary heat source in electric vehicles.

The performance and durability of the Lithium-ion battery pack is limited by its operating temperature. Several studies have accounted for the effect of high operating temperatures on the reduced performance and life of Lithium-ion batteries [10–13]. Lithium-ion batteries have an ideal operating temperature window between $15°C$ and $40°C$. Additionally, the temperature variation between different cells of the battery pack is ideally to be limited below $5°C$ to ensure an optimal balance between durability and performance [14–16]. The aforementioned thermal requirements are difficult to achieve under aggressive drive cycles, fast battery charging, and high ambient temperature conditions. An ideal thermal management system should be capable of maintaining the battery pack at the optimum average temperature for all vehicle operating conditions, with only minor temperature variations between the cells of the battery pack. Failure to achieve the required thermal operating conditions for the battery pack, may lead to reduced battery life or battery thermal runaway failure [17–20].

Therefore, to support the increase in driving range, improve customer adoption, and ensure passenger safety, the thermal management system must be developed in tandem with advancements in battery technology.

1.2 Automotive thermal management system

A generic schematic of an automotive thermal management system is illustrated in Fig. 1.1. A liquid coolant is circulated over the battery pack and other peripheral underhood components. The coolant is then circulated through a pump to increase its pressure before being directed through the channels of a heat-exchanger. Ambient air is allowed into the heat-exchanger, facilitating the forced-convective heat transfer between the coolant circulating within the channels of the heat-exchanger and the ambient air. The ambient air acts as the heat sink. Once the heat rejection process is complete, the coolant recirculates back over the underhood components, closing the loop. However, ambient air cannot naturally flow through the heat-exchanger due to the flow resistance offered by the heat-exchanger. Typically, a low-pressure fan is used to overcome this flow-resistance and move air between the channels of the heat-exchanger.

Low-pressure axial fans are ideal for applications which require the delivery of a large volume flowrate of air at a moderate pressure rise, such as cooling and ventilation applications [21]. The fan can be positioned either upstream or downstream of the heat-exchanger, i.e., the fan can either push/pull air through the heat-exchanger. The cooling-fans are typically operational at low-vehicle speeds ($< 30\ km/h$). At higher vehicle speeds the cooling is achieved through the high velocity ram-air entering the underhood region, and the fan "free-wheels". Consequently, the cooling-fan acts as a

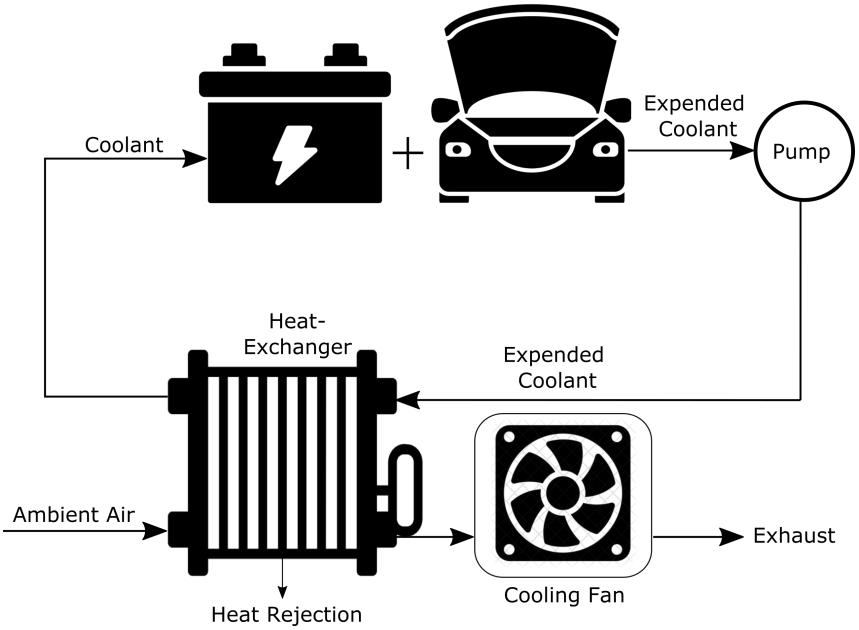

Figure 1.1: Schematic of a generic automotive thermal management system

flow blockage to any downstream components, in particular the hub on which the rotor blades are mounted.

The convective heat transfer rate (H in Watts) between the ambient air and the liquid coolant circulating through the heat-exchanger is influenced by: the mass flowrate of air moving through the heat-exchanger ($\dot{m}$ in kg/s), the specific heat capacity of air (c_p in J/kgK), and the temperature difference between the ambient air and the liquid coolant (ΔT in K). Therefore, it follows from Eq. (1.1), that the convective heat-transfer rate (H) between the ambient air and the liquid coolant is directly proportional to the mass flowrate of air being forced through the heat-exchanger.

Additionally, from Eq. (1.1), it can also be concluded that the temperature of the ambient air plays a critical role in the cooling-fan's ability to act as a heat sink. At higher ambient temperatures, a larger mass flowrate of air is required to compensate for the reduced temperature difference (ΔT) between the ambient air and the coolant in the heat-exchanger. Since the specific heat and thermal conductivity of air is much lower than that of a typical liquid coolant (10% and 25%, respectively), forced convective cooling by air is the limitation in the heat rejection process. Hence, increasing the airflow is decisive for the cooling performance. Consequently, the cooling-fan is the limiting factor and key to meeting the thermal requirements. Additionally, since the cooling-fan, is a power consuming device, increasing its aerodynamic efficiency reduces its parasitic energy consumption.

In ICE powered vehicles, cooling fans are mounted on and powered by the crankshaft. However, since electric vehicles do not have a crankshaft, their cooling fans are instead driven by electric motors housed within their respective hubs. As a result, they are often referred to as electric fans or "E-Fans." In most cases, automotive cooling fans are low-pressure axial fans, i.e., they operate in the incompressible flow

regime, generate a low to moderate pressure rise, and primarily generate flow parallel to their rotational axis [22].

$$H = \dot{m} \cdot c_p \cdot \Delta T \tag{1.1}$$

1.3 The E-Fan 1 project

The thermal management requirements of ICE powered vehicles currently influence the design of automotive cooling-fans. The existing off-the-shelf cooling-fans do not meet the thermal requirements of commercial electric vehicles, which makes it essential to develop a new generation of cooling-fans specifically designed for electric vehicles. Additionally, the absence of a transmission, exhaust system, and the ICE in electric vehicles eliminates the characteristic masking noise produced by it [23]. This leads to an increased prominence of the noise produced by other underhood components. At low vehicle speeds and during fast charging of a stationary vehicle, the noise produced by the cooling-fan, and its electric-motor can be a significant source of cabin noise, and passenger annoyance [24]. At higher speeds, wind noise and tire-road interaction noise dominate [23], and consequently mask the noise from the cooling-fans. Therefore, for electric vehicles both the aerodynamic and acoustic performance of the cooling-fan is of significance, in particular at low vehicle speeds.

The current generation of cooling-fans are typically designed and tested under ideal, clean inlet flow conditions on test rigs, free from spatial or temporal disturbances. However, when installed in the tightly packed underhood region, these cooling-fans typically ingest spatially non-uniform flow. The ram air entering the underhood region typically passes through the grill, charger cooler, and heat-exchanger before being ingested by the cooling fan, i.e., the cooling-fan is often subjected to several upstream blockages. Additionally, to accommodate the cooling-fan into tight underhood spaces, the axial length of the fan is often limited. To ensure that the cooling-fan fits into the required space, the standard inlet bellmouth responsible for conditioning the flow incident on the rotor blades is often removed or shortened. This leads to a sharp lip intake which further spatially distorts the flow incident on the rotor blade, especially at the rotor tip region. Several scientific studies have illustrated, through both numerical and experimental investigations, the detrimental effect on the aerodynamic and aeroacoustic performance of low-pressure axial fans ingesting spatially non-uniform flow [25–30] and/or turbulent inflow [31–37]. The first goal of the *E-Fan 1* project is to extend the previous work done with regard to the effect of ingesting spatially non-uniform flow, to fans representative of those used in automotive cooling systems through Computational Fluid Dynamics (CFD) and Computational Aero-Acoustics (CAA) investigations. Consequently, also evaluate the suitability of a variety of numerical methods of different fidelity to accurately capture the installation effects by comparing numerical data to publicly available experimental data.

Additionally, in most current automotive cooling solutions, multiple low-pressure axial fans are placed in parallel instead of using a single large-diameter fan. The required mass flowrate of air through the heat-exchanger can be delivered by either

a single large-diameter fan or multiple smaller-diameter fans. In the low-speed, incompressible flow regime in which these cooling-fans typically operate, air density remains constant, i.e., the mass flowrate is equivalent to volume flowrate (Q in m^3/s). According to fan laws, the volume flowrate of air delivered by the fan scales with the cube of the fan diameter ($Q \propto d_{fan}^3$) [22, 38], i.e., a small increase in fan diameter can result in a substantial increase in volume flowrate of air delivered by the fan. However, spatial constraints often limit the fan diameter, making configurations with multiple smaller-diameter fans arranged in parallel in a modular fashion, the preferred choice. In a parallel setup, the rotational axes of the fans are parallel to one another, and they have identical axial positions.

The parallel fan arrangement offers several advantages over a stand-alone single fan setup. A parallel fan setup of multiple small-diameter fans can achieve a more uniform airflow distribution downstream of the cooling-fans. Additionally, the smaller hub diameter associated with small-diameter fans reduces flow blockage to downstream components at high vehicle speeds—especially when cooling is achieved through ram-air while the fans remain stationary. Each fan in a parallel setup is powered by an independent electric motor, allowing individual control based on cooling requirements. Limited scientific research exists on the aerodynamic and aeroacoustic performance of cooling-fans placed in parallel. Most research with regard to low-pressure axial fans in parallel are restricted to underground mining fans [39, 40] or heating, ventilation, and air conditioning (HVAC) fans [41] which do not have the dimensional or operational resemblance to automotive cooling-fans, highlighting the need for further investigations into the aerodynamic and aeroacoustic behavior of fans placed in parallel. The *E-Fan 1* project, in addition to the previously stated goals, also aims to numerically investigate the aerodynamic and acoustic effect of placing low-pressure axial fans in parallel.

1.4 Thesis outline and scope

This thesis is divided into two parts: the introductory chapters and the appended papers. The introductory chapters present the fundamentals associated with the aerodynamics and aeroacoustics of low-pressure axial fans with a stationary shroud. The framework for an in-house python library, *C-Fan*, developed as a part of this thesis work, is also detailed as a part of the introductory chapters.

Chapter. 2 and chapter. 3, respectively discuss the fundamentals of the aerodynamics and aeroacoustics of low-pressure axial fans. Chapter. 4 presents the design methodology for low-pressure axial fans using the Blade Element Momentum (BEM) method for low-solidity fans to generate a series of four rotor blade designs with different blade-loading distributions. The framework for the in-house Python library *C-Fan*, developed as part of this thesis work, is also detailed in chapter. 4. A summary of the appended papers is presented in chapter. 5.

The aerodynamic and aeroacoustic installation effects of low-pressure axial fans in the underhood region are investigated in the appended papers. Paper-1 computationally examines the effect of an upstream blockage on the aerodynamic performance of a low-pressure axial fan. Paper-2 computationally evaluates the aerodynamic

performance of two ducted low-pressure axial fans with a stationary shroud installed in parallel. Paper-3 numerically investigates the aeroacoustic performance of two low-pressure axial fans when installed in parallel. Paper-4 examines the effect of the inlet bellmouth dimensions on the tip-noise of a low-pressure axial fan. Paper-5, computationally investigates the effect of the aerodynamic operating point on the aeroacoustic performance of an in-service automotive cooling fan with a rotating ring. Additionally, in paper-5, the effect of a circumferential upstream blockage, blocking a 60° sector of the fan inlet face is computationally evaluated and compared against experimental data. Paper-6, investigates the aerodynamic performance of the four rotor blade designs, presented in chapter. 4 when subjected to non-uniform inlet profiles. A non-uniform inlet profile similar to that obtained from the work performed in paper-1, is utilized. Additionally, the aeroacoustic performance of the four different rotor blade designs under spatially uniform inflow conditions is also investigated numerically in paper-6.

A steady-state, Reynolds-Averaged Navier Stokes (RANS) analysis is performed in paper-1 on a single-blade passage. A full-annulus, Unsteady RANS (URANS) analysis is carried out in paper-2. A full-annulus, unsteady, Delayed Detached Eddy Simulation (DDES), hybrid CAA analysis is carried out in papers 3 - 6

For papers 1 - 4, a ducted, low-pressure axial fan, with a stationary shroud designed by Friedrich Alexander University (FAU) is used [42, 43]. For paper-5, an in-service automotive cooling fan with a rotating ring is used. Paper-6, investigates four different rotor designs generated using in-house python code *C-Fan*.

Overall, this thesis computationally evaluates four different installation effects, six different rotor designs of ducted low-pressure axial fans, using three different fidelity of numerical methods, see Fig. 1.2.

1.4.1 State of the art

Paper-2 and paper-3 present a detailed investigation of the aerodynamic and aeroacoustic performance of two low-pressure axial fans installed in parallel. Although low-pressure axial fans have been widely studied, limited scientific work is available with regard to the aerodynamic and aeroacoustic performance of fans installed in parallel. Most research on parallel fan setups has been conducted for underground mining fans [39, 40] or for fans used in HVAC systems [41]. However, HVAC fans are typically centrifugal fans and therefore not relevant to the cooling-fans used in automotive thermal management systems. While underground mining fans are axial, they lack both the dimensional and operational relevance to automotive cooling fans. The limited prior research on the aerodynamic and aeroacoustic performance of low-pressure axial fans installed in parallel, underlines the state-of-the-art contribution of this work.

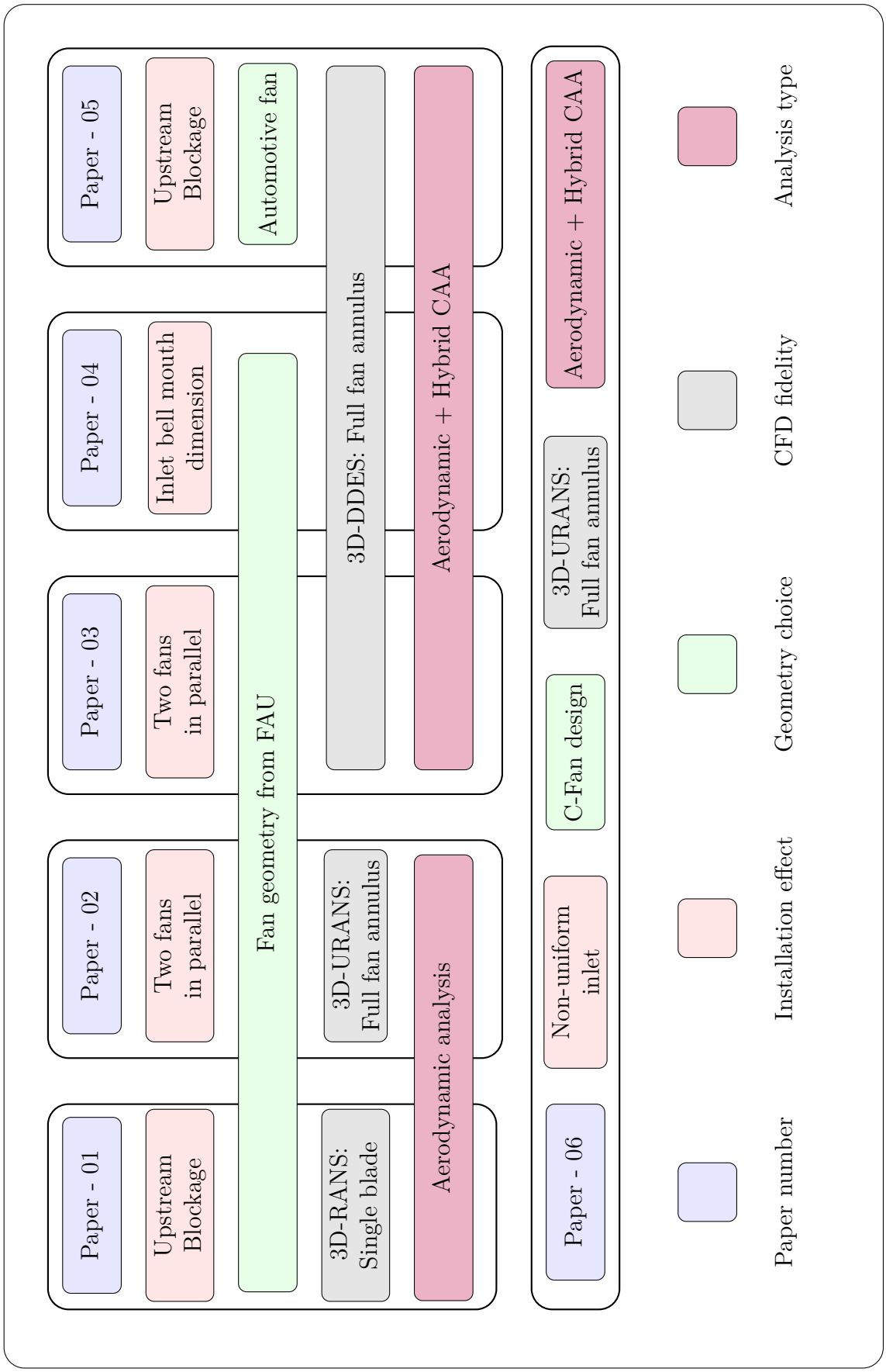

Figure 1.2: Appended papers overview

Chapter 2

Low Pressure Axial Fans - Aerodynamics

This chapter outlines the fundamentals associated with the aerodynamic performance of low-pressure axial fans and describes the methodology for the aerodynamic design of rotor blades using the Blade Element Momentum (BEM) method for low-solidity fans [38, 44]. The theory presented here is subsequently applied to design a series of four fans in chapter. 4, with different blade-loading distributions. The designs presented in chapter. 4 are computationally investigated in Paper-6.

2.1 Turbomachine classification

Turbomachines transfer energy to or from a continuously moving fluid through the dynamic action of moving blade rows by changing the stagnation enthalpy of the fluid. Turbomachines are broadly classified as turbines or pumping devices, depending on the direction of energy transfer. Pumping devices absorb power and increase the pressure or head of the fluid. Alternatively, a turbine produces energy by expanding the fluid to a lower pressure or head. Turbomachines are further classified based on the flow direction at the rotor outlet. If the flow direction at the rotor outlet is primarily parallel to its rotational axis, it is classified as an axial-flow machine. Alternatively, if the flow direction at the rotor outlet is predominantly perpendicular to the rotational axis, it is classified as a radial-flow machine. Finally, if the flow direction at the rotor outlet has significant axial and radial components, it is classified as a mixed-flow machine. Based on the operation regime, turbomachines are classified as either compressible or incompressible machines. A turbomachine is considered to be operating in the incompressible flow regime, if the Mach number (Ma) is below 0.3, and the density change ($\Delta\rho/\rho$) is below 5% everywhere within the turbomachine. The classification of turbomachines is illustrated in Fig. 2.1.

Low-pressure axial fans are classified as incompressible, axial, pumping devices. The distinction between a fan and a compressor can be made on the basis of maximum work performed per unit massflow of air through the pumping device. For a fan, the maximum work performed per unit massflow of air through it, is set to 25 kJ/kg [45]. Low-pressure axial fans can further be categorized into propeller fans (no

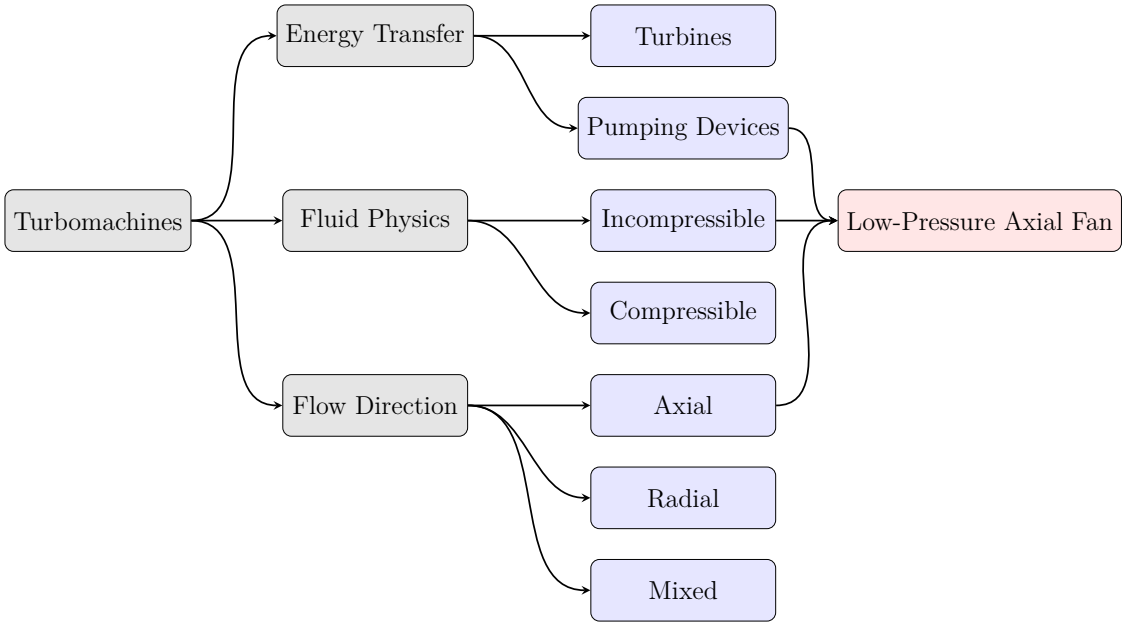

Figure 2.1: Flowchart illustrating the classification of turbomachines

casing), axial fans with casing and no guide vanes (ducted-axial fans), and axial fans with outlet guide vanes (vane-axial fans). This work focuses on ducted-low pressure axial fans, with the exception of Paper-5, which uses a geometry from an in-service automotive cooling fan with a rotating ring and outlet guide vanes, i.e., vane-axial fan.

2.2 Fan aerodynamic performance parameters

The aerodynamic operating point of a low-pressure axial fan is quantified by its rotational speed (ω in rad/s) and ingested mass flowrate ($\dot{m}$ in kg/s). For a fan operating in the incompressible flow regime, the volume flowrate of air (Q in m^3/s) ingested by the fan is used to quantify the operating point, instead of the mass flowrate as the density (ρ in kg/m^3) remains constant.

At a specified aerodynamic operating point, the aerodynamic performance of the fan is quantified by the total-to-total pressure rise (p_{tt} in Pa) achieved by the fan, and its total-to-total efficiency (η_{tt}). The total-to-total pressure rise is calculated as the difference in the massflow averaged total pressure at the fan exit ($p_{t,exit}$) and the fan inlet ($p_{t,inlet}$), according to Eq. (2.1). The total pressure is the sum of the dynamic and static pressure. However, when the fan is the last component of a system and exhausts freely into atmospheric conditions, the dynamic pressure of the jet exiting the fan constitutes a loss. Therefore the dynamic pressure at the fan outlet is not accounted for in the effective pressure increase achieved by the fan. In this case, the effective pressure rise achieved by the fan is reported by neglecting the dynamic pressure at the exit. The total-to-static pressure rise (p_{ts} in Pa) is instead used to report the effective pressure increase, according to Eq. (2.1), where $p_{st,exit}$ is the area-averaged static pressure at the fan outlet.

$$p_{tt} = (p_{t,exit} - p_{t,inlet}) \qquad p_{ts} = (p_{st,exit} - p_{t,inlet}) \tag{2.1}$$

The corresponding aerodynamic efficiency of the fan is calculated according to Eq. (2.2). When the fan is exhausting into atmospheric conditions the efficiency is reported as the total-to-static efficiency (η_{ts}), and is calculated using the total-to-static pressure. In Eq. (2.2), the shaft power (P_{shaft} in W) is calculated as the product of the rotational speed and the shaft torque (T_{shaft} in Nm). Alternatively, the total-to-total efficiency is calculated using the total-to-total pressure, according to Eq. (2.2).

$$\eta_{tt} = \left(\frac{Q\ p_{tt}}{P_{shaft}}\right) \qquad \eta_{ts} = \left(\frac{Q\ p_{ts}}{P_{shaft}}\right) \qquad P_{shaft} = (\omega\ T_{shaft}) \tag{2.2}$$

The regime of operation of a turbomachine is quantified by the Mach Number (Ma) and the Reynolds number (Re), calculated according to Eq. (2.3), where ν is the kinematic viscosity and c_o is the speed of sound. Low-pressure axial fans operate in the incompressible and turbulent flow-regime. For low viscosity flows at high speeds ($Re > 2 * 10^5$), the effect of Reynolds number on turbomachine performance is low [46]. This is attributed to the formation of very thin and turbulent viscous boundary layers around the rotor blade surface, which have minimal effect on the global flow field. However it is noted that for automotive cooling fans, which typically have small diameters and rotate at low-speeds, the chord-based Reynolds number does not always meet this criteria [38, 42, 47–51].

$$Re = \left(\frac{\omega\ d_{fan}^2}{4\nu}\right) \qquad Ma = \left(\frac{\omega\ d_{fan}}{2c_o}\right) \tag{2.3}$$

Non-dimensional parameters are often used to quantify the aerodynamic operating point and aerodynamic performance of turbomachines. Non-dimensional numbers enable the comparison between geometrically similar turbomachines, different operating conditions, and comparison between experimental and numerical data. For a turbomachine operating in the incompressible flow regime, the non-dimensional numbers are expressed in terms of control variables (n and Q), geometric variables (d_{fan}), and fluid flow properties (ρ). The two non-dimensional coefficients of interest, are the flow coefficient (φ), and the pressure coefficient (ψ). Each non-dimensional number is expressed as a combination of the control variables, geometric variables and flow properties, in Eq. (2.4) [22, 38]. Here, it is also important to note the difference in the definition of non-dimensional parameters in German and English literature. For this work, the German definition of the non-dimensional coefficients has been used [38, 52]. In Eq. (2.4), the rotational speed (n) is represented rotations per second (rps).

$$\varphi = \left(\frac{4\ Q}{\pi^2\ n\ d_{fan}^3}\right) \qquad \psi = \left(\frac{2\ p_{tt}}{\pi^2 \rho\ n^2\ d_{fan}^2}\right) \tag{2.4}$$

To determine the aerodynamic operating range of any given fan, a speed-line is constructed. In order to obtain a speed-line for a fan, as shown in Fig. 2.2, the

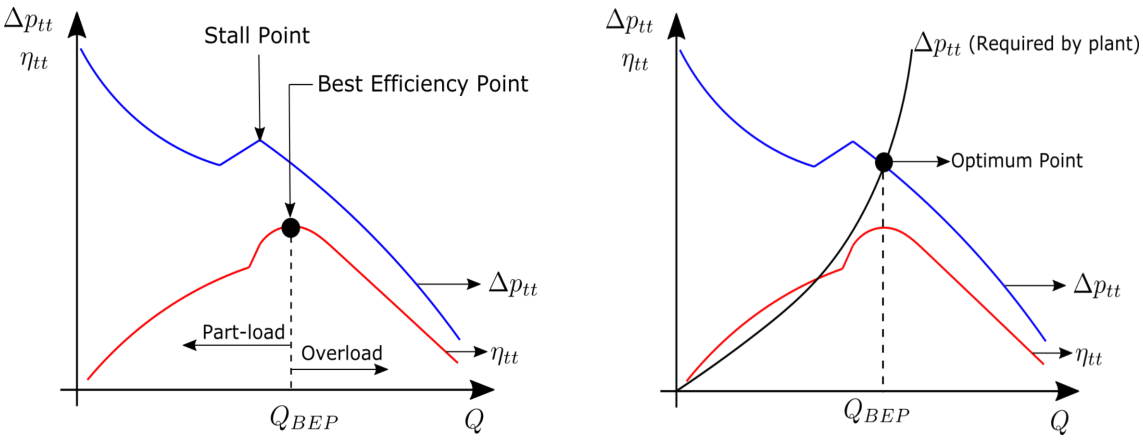

Figure 2.2: Aerodynamic characteristic curve for a fixed rotational speed of the fan (**left**) with characteristic curve for the cooling system included (**right**), adapted from [38].

volume flowrate of air ingested by the fan is changed while keeping the fan's rotational speed constant. The pressure rise and efficiency of the fan increase with the decrease in the volume flowrate of air until a specific point referred to as the Best Efficiency Point (BEP). At the BEP, the fan operates at its peak aerodynamic efficiency. If the fan operates at a volume flowrate greater than the BEP, it is considered to be operating in overload conditions. Alternatively, if the fan operates at a volume flowrate smaller than the BEP, it is considered to be operating at part-load condition. When the volume flowrate of air being ingested by the fan is smaller than the point at which stall occurs, see Fig. 2.2, large-scale separations occur on the blade surface, which results in an abrupt decrease in fan efficiency and a substantial increase in the noise produced by the rotor blade.

2.3 System level fan design parameters

This section outlines the details of the basic design parameters obtained from the cooling system requirements, which is used as input for the rotor blade design process.

2.3.1 System requirement

The fan design process begins with identifying the system requirements the fan must satisfy. For an automotive thermal management system, this entails:

- Determining the volume flowrate (Q_{target} in m^3/s) of air required for rejecting heat from the expended coolant in the heat-exchanger.
- Determining the maximum fan diameter (d_{fan} in m) that can be accommodated into the available space in the underhood region. The choice of fan diameter is motivated by the size and shape of the heat-exchanger. The choice of using a single-fan or a multi-fan setup plays a crucial role when choosing the maximum fan diameter.

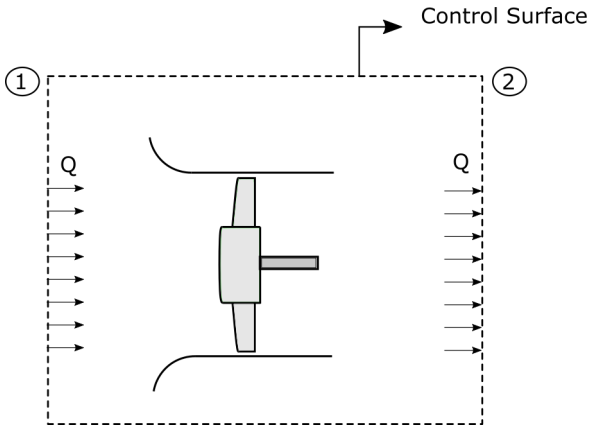

Figure 2.3: Schematic of a fan placed upstream of heat exchanger, within control volume

.

- Determining the total-to-total pressure increase ($\Delta p_{tt,req}$ in Pa) the fan must achieve for the specified volume flowrate. The total-to-total pressure increase required to be achieved by the fan is motivated by the flow resistance offered by the upstream/downstream heat-exchanger.
- Determining the typical operating conditions of the vehicle, i.e., the ambient pressure (P_∞ in Pa) and ambient temperatures (T_∞ in K) the vehicle is most likely to operate in.

Figure 2.3 illustrates an arbitrary fan, with station-1 and station-2 marking the control surface boundaries around the fan. Flow enters through station-1 and exits through station-2. Between station-1 and station-2, the fan must achieve a total pressure increase of $\Delta p_{tt,req}$, according to Eq. (2.5). The fan must compensate for total pressure losses in the system due to ancillary components, i.e., these losses must be accounted for in the required total pressure rise the fan must achieve. Pressure losses from components like the casing, diffuser, and ducts are calculated according to Eq. (2.6). The pressure loss coefficient (ξ) for different ancillary component can be found in standard literature [53].

The total-to-total pressure increase that the fan is required to achieve can also be plot as a characteristic curve, as illustrated in Fig. 2.2. Since all velocities in Eq. (2.5) and Eq. (2.6), are proportional to the volume flowrate, the characteristic curve for the total-to-total pressure increase that the fan is required to achieve, is best approximated as a quadratic curve, see Fig. 2.2 [38]. Ideally a fan must be designed such that its peak efficiency point, coincides with the most likely to occur vehicle cooling requirement cycle, while still being sufficiently robust to handle off-design conditions, i.e., overload and part-load conditions.

$$\Delta p_{tt,req} = (p_2 - p_1) + \frac{\rho}{2}(c_2^2 - c_1^2) + \Sigma \Delta p_{loss} \tag{2.5}$$

$$\Delta p_{loss} = \xi \left(\frac{\rho c^2}{2} \right) \tag{2.6}$$

2.3.2 Fan type selection

The type of fan (axial, radial, or, mixed) best suited to satisfy the system requirements, is made using the Cordier diagram, see Fig. 2.4. The Cordier diagram [54] is a tool for selecting the optimal fan-type based on specific-speed (σ) and specific-diameter (δ). The specific-speed and specific-diameter are calculated according to Eq. (2.7) and Eq. (2.8), respectively. Specific-speed and specific-diameter are not independent dimensionless numbers, but are instead dependent on the flow coefficient (φ) and pressure coefficient (ψ).

The Cordier diagram was derived empirically from measurement data. The specific-speed and specific-diameter were calculated for the operating point with the highest efficiency for a range of rotor types. These points were plotted into the Cordier diagram, resulting in a band that represents the optimal fan-type for a given specific-speed and specific-diameter. This optimal range is represented by the gray-colored band in Fig. 2.4. Axial fans are high specific-speed ($\sigma_{opt} > 0.6$) and low specific-diameter ($\delta_{opt} < 0.3$) turbomachines [22, 38].

$$\sigma = \frac{(2\pi^2)^{\frac{1}{4}}\ n\ \rho^{\frac{3}{4}}\ Q^{\frac{1}{2}}}{p_{tt}^{\frac{3}{4}}} = \varphi^{\frac{1}{2}}\ \psi_{tt}^{-\frac{3}{4}} \tag{2.7}$$

$$\delta = \frac{d_{fan}\ p_{tt}^{\frac{1}{4}}}{(8/\pi^2)^{\frac{1}{4}}\ \rho^{\frac{1}{4}}\ Q^{\frac{1}{2}}} = \varphi^{-\frac{1}{2}}\ \psi_{tt}^{\frac{1}{4}} \tag{2.8}$$

Figure. 2.5 and 2.6 illustrate the speed-lines for an axial and radial machine for a given specific-speed and diameter [38]. The radial machine ($\sigma = 0.4$) achieves a higher total-to-total pressure coefficient (ψ_{tt}) for a given flow coefficient compared to an axial fan. However, the radial machine has a smaller range of operation compared to an axial machine, i.e., the range of flow coefficient (φ), it can operate over without inducing stall. It is also noted that in Fig. 2.5, the peak total-to-total efficiency ($\eta_{tt,max}$) for the axial fan is achieved at a higher flow-coefficient compared to the radial fan.

For automotive cooling systems, the volume flowrate of air delivered by the cooling-fan is crucial. Ideally, the cooling-fan must be designed such that the peak aerodynamic efficiency point is at the highest possible volume flowrate. Due to the large range of operating conditions over which the vehicles must operate, axial fans which are capable of delivering high volume flowrates of air at moderate pressure rises is the preferred choice over radial and mixed flow machines.

2.4 Axial fan blade cascade

The flow kinematics of an axial fan/compressor rotor stage can be detailed using velocity triangles on an elemental-blade-cascade. An elemental-blade-cascade is obtained by segmenting a rotor using co-axial cylindrical surfaces, separated by a radial distance (δr), as illustrated in Fig. 2.7. The resulting elemental-blade-cascade has an inlet area, δA. A single elemental-blade-cascade at a specified radius is comprised of of individual blade-elements equal to the number of rotor blades. The

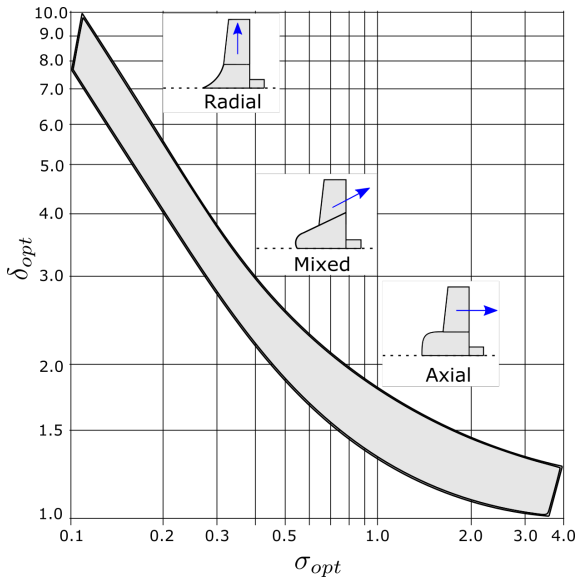

Figure 2.4: Cordier Diagram, adapted from [54].

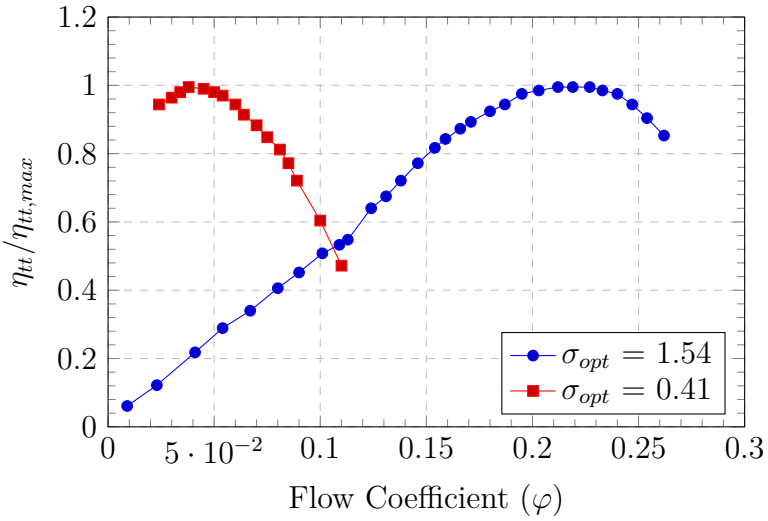

Figure 2.5: Comparison between normalized total-to-total efficiency of an axial fan ($\sigma_{opt} = 1.54$) and radial fan ($\sigma_{opt} = 0.41$), adapted from [38].

inlet and outlet velocity triangles for an axial fan/compressor elemental-blade-cascade is illustrated in Fig. 2.8.

All velocity components denoted by, c, and angles by, α, are with respect to the absolute frame of reference. All velocity components denoted by, w, and angles by, β, are with respect to the rotational frame of reference. The absolute velocity ($\overrightarrow{c}$) is the vector sum of the blade velocity (U) and the relative velocity ($\overrightarrow{w}$), according to Eq. (2.9). The blade velocity is constant for an elemental-blade-cascade, and is the product of the rotational speed of the rotor (ω) and the radius of the elemental-blade-cascade (r).

$$\overrightarrow{c} = (U + \overrightarrow{w}) \tag{2.9}$$

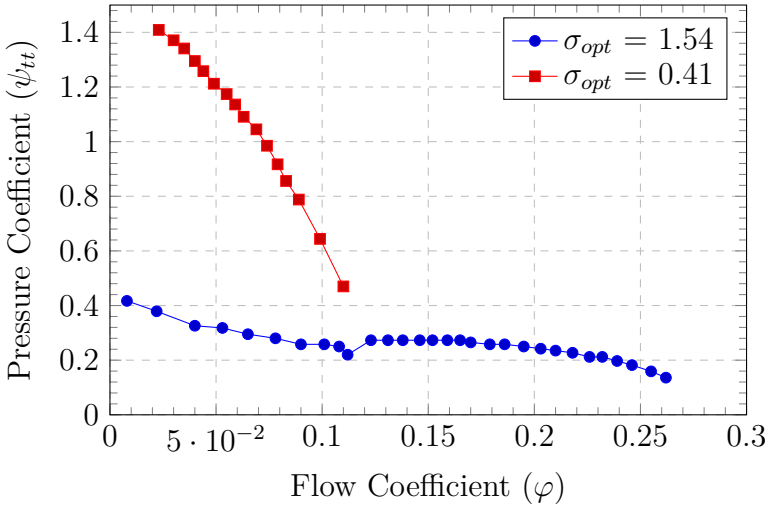

Figure 2.6: Comparison between normalized total-to-total pressure of an axial fan ($\sigma_{opt} = 1.54$) and radial fan ($\sigma_{opt} = 0.41$), adapted from [38].

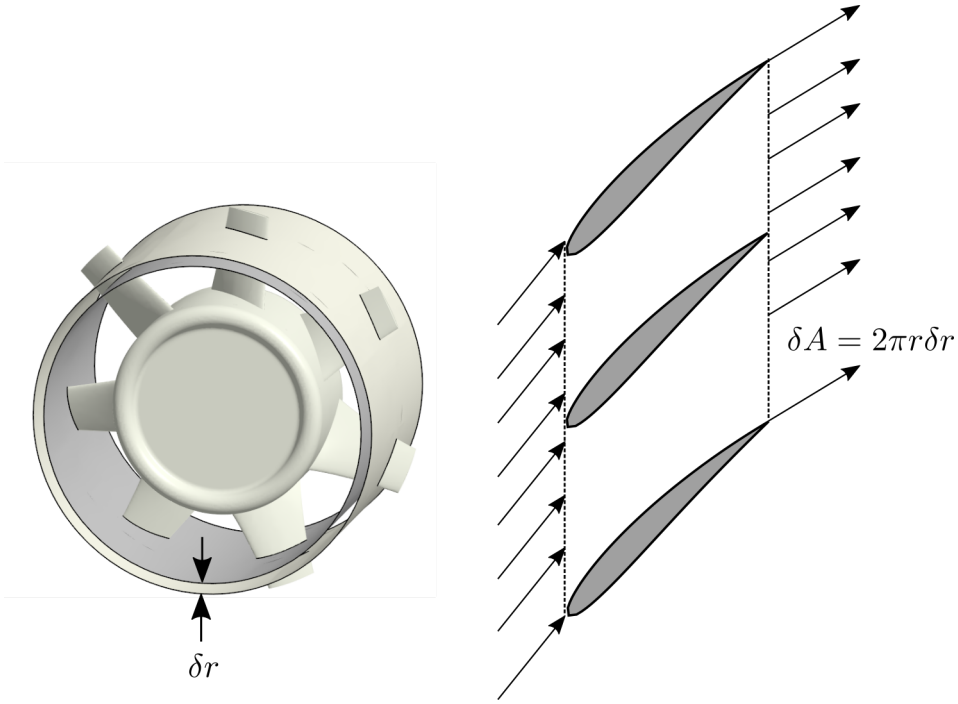

Figure 2.7: A rotor segmented using co-axial cylinders, separated by a radial distance (δr) (**left**). Elemental-blade-cascade with three blade elements (**right**).

Both the absolute velocity and relative velocity are the vector sum of their respective axial, radial and circumferential velocity components, according to Eq. (2.10). The meridional velocity which acts in the rz plane is the vector sum of the axial and radial velocity components, according to Eq. (2.11). For an axial fan, the meridional velocity component remains constant between rotor inlet and outlet, i.e., $\overrightarrow{c_{m,1}} = \overrightarrow{c_{m,2}}$. For a purely axial fan operating at its Aerodynamic Design Point (ADP), the radial velocity component both at rotor inlet and outlet should be zero, i.e., the meridional

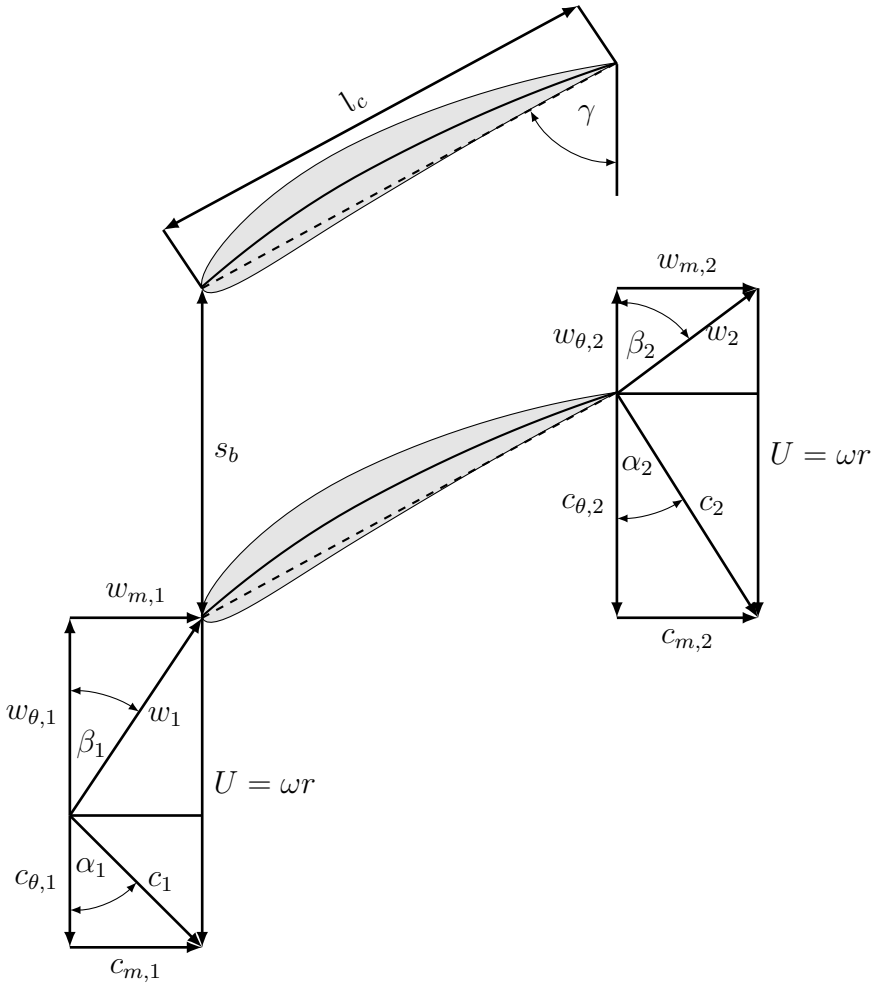

Figure 2.8: Inlet ($\bullet_1$) and outlet ($\bullet_2$) velocity triangles illustrated on an elemental-blade-cascade with two blade-elements for an axial fan/compressor.

velocity component is equal to the axial velocity component ($\overrightarrow{c_m} = \overrightarrow{c_{ax}}$).

$$\overrightarrow{c} = (\overrightarrow{c_{ax}} + \overrightarrow{c_{rad}} + \overrightarrow{c_\theta}) \qquad \overrightarrow{w} = (\overrightarrow{w_{ax}} + \overrightarrow{w_{rad}} + \overrightarrow{w_\theta}) \tag{2.10}$$

$$\overrightarrow{c_m} = (\overrightarrow{c_{ax}} + \overrightarrow{c_{rad}}) \qquad \overrightarrow{w_m} = (\overrightarrow{w_{ax}} + \overrightarrow{w_{rad}}) \tag{2.11}$$

Since the blade velocity, by definition acts only in the tangential direction (θ in Fig. 2.8), there is no change in the axial and radial velocity component when moving from the stationary frame of reference to the relative frame of reference, according to Eq. (2.12). The circumferential velocity component in the relative frame of reference ($\overrightarrow{w_\theta}$) is calculated as the difference in the absolute circumferential velocity component ($\overrightarrow{c_\theta}$) and blade velocity ($U$), according to Eq. (2.13).

$$\overrightarrow{c_{ax}} = \overrightarrow{w_{ax}} \qquad \overrightarrow{c_{rad}} = \overrightarrow{w_{rad}} \qquad \overrightarrow{c_m} = \overrightarrow{w_m} \tag{2.12}$$

$$\overrightarrow{w_\theta} = (\overrightarrow{c_\theta} - U) \tag{2.13}$$

The absolute and relative flow angle at the rotor inlet (α_1, β_1) or rotor outlet (α_2, β_2) is calculated as the ratio of the magnitude of the meridional and circumferential component of velocity, according to Eq. (2.14). Here, it is noted that there is a difference in the convention for angle notations in popular literature. In this work, the flow angles (α and β) are taken with respect to the circumferential flow-direction. In several other literature [22], the angles are defined with respect to the axial flow-direction.

$$\alpha = tan^{-1}\left(\frac{c_m}{c_\theta}\right) \qquad \beta = tan^{-1}\left(\frac{c_m}{c_\theta - U}\right) \tag{2.14}$$

As the fluid moves through the rotor blade passage of an axial fan/compressor, the rotor blade performs work on the flow by turning the flow and consequently diffusing the flow to a lower velocity and higher pressure.

As a result of the flow being turned, the relative flow angle (β) at the rotor outlet is larger than at the rotor inlet ($\beta_2 > \beta_1$). Furthermore, as a result of diffusing the flow through the rotor blade passage, the magnitude of the relative flow velocity decreases ($w_2 < w_1$). A decrease in the relative velocity at the rotor outlet (w_2) ultimately leads to the circumferential velocity component at rotor outlet to be larger in magnitude than at the rotor inlet ($c_{\theta,2} > c_{\theta,1}$).

From Euler's turbomachinery equation, the specific work done on the fluid by all blade-elements in an elemental-blade-cascade ($Y_{t,ca}$) at specific blade radius, is the product of the blade velocity and the change in the circumferential velocity component, according Eq. (2.15), where the subscript, $\bullet_{\text{ca}}$, represents a single elemental-blade-cascade.

Typically low-pressure axial fans do not have inlet guide vanes [42, 47–51, 55–57], i.e., the flow entering the rotor has zero circumferential velocity component ($\overrightarrow{c_{\theta,1}} = 0$). The total-to-total pressure rise ($\Delta p_{tt,ca}$) achieved by a single elemental-blade-cascade is the product of the specific work done and the flow density, according to Eq. (2.15).

$$Y_{t,ca} = U(c_{\theta,2} - c_{\theta,1}) \qquad \Delta p_{tt,ca} = \rho\, Y_{t,ca} \tag{2.15}$$

The maximum achievable, total specific work by the blade ($Y_{t,B}$) and the total-to-total pressure rise achieved by the blade ($p_{tt,B}$) is obtained through a summation over all elemental-blade-cascades along the rotor blade span, according to Eq. (2.16), where δQ_{ca}, is volume flowrate of air entering the elemental-blade-cascade through inlet area, δA, in Fig. 2.7. During the design process the the hydraulic losses, must be taken into consideration. Ultimately, the design target total-to-total pressure (p_{tt}) that the rotor blade must achieve is calculated, according to Eq. (2.17), where, η_h, is the hydraulic efficiency. The hydraulic efficiency is a measure of how much work is actually transferred to the fluid.

$$Y_{t,B} = \frac{1}{Q_B}\sum_{ca}(Y_{t,ca}\ \delta Q_{ca}) \tag{2.16}$$

$$p_{tt,B} = (\rho Y_{t,B}) \qquad p_{tt} = (\eta_h\ p_{tt,B}) \tag{2.17}$$

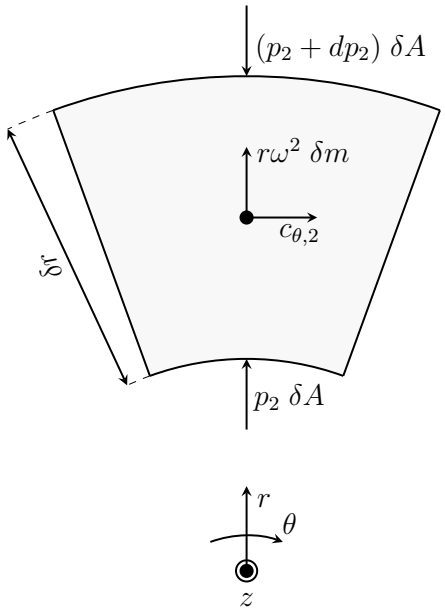

Figure 2.9: Radial forces acting on an elemental mass (δm) on a plane downstream of the rotor (**right**), adapted from [43].

2.5 Flow kinematics - Radial equilibrium

For a purely axial fan operating at its ADP, the radial velocity component should ideally be zero at both the rotor inlet and outlet ($\overrightarrow{c_{rad,1}} = \overrightarrow{c_{rad,2}} = 0$). To achieve radial-equilibrium, the net radial forces acting on a fluid element passing through the rotor must be zero. A zero radial velocity component ensures that the flow streamlines lie on co-axial cylindrical surfaces as illustrated in Fig. 2.7.

In Fig. 2.9, a plane just downstream of the rotor is illustrated. A small fluid element with elemental mass (δm) which is considered to be positioned on this rotor downstream plane, experiences pressure and centrifugal forces in the radial direction. The centrifugal force (F_c) experienced by the elemental mass is calculated according to Eq. (2.18). To achieve radial equilibrium, the sum of the radial forces acting on the element mass must be zero, according to Eq. (2.19). Replacing values of δm and ω in Eq. (2.19), yields Eq. (2.20).

$$F_c = \Big(r\omega^2 \delta m\Big) \qquad \delta m = (\rho \delta A \delta r) \qquad \omega = \left(\frac{c_{\theta,2}}{r}\right) \tag{2.18}$$

$$\Big(p_2 \delta A - (p_2 + dp_2)\delta A + r\omega^2 \delta m\Big) = 0 \tag{2.19}$$

$$\frac{dp_2}{dr} = \rho \left(\frac{c_{\theta,2}^2}{r}\right) \tag{2.20}$$

The total pressure on the rotor downstream plane ($p_{t,2}$) is defined as the sum of the static and dynamic component, according to Eq. (2.21).

$$p_{t,2} = p_2 + \left(\frac{\rho c_2^2}{2}\right) = p_2 + \frac{\rho}{2}(c_{\theta,2}^2 + c_{m,2}^2) \tag{2.21}$$

Differentiating Eq. (2.21) with respect to r, yields Eq. (2.22).

$$\frac{dp_{t,2}}{dr} = \frac{dp_2}{dr} + \rho\left(c_{\theta,2}\frac{dc_{\theta,2}}{dr} + c_{m,2}\frac{dc_{m,2}}{dr}\right) \tag{2.22}$$

Substituting (dp_2/dr), from Eq. (2.20) into Eq. (2.22), yields Eq. (2.23).

$$\frac{dp_{t,2}}{dr} = \left(\rho\frac{c_{\theta,2}^2}{r} + \rho c_{\theta,2}\frac{dc_{\theta,2}}{dr}\right) + \rho c_{m,2}\frac{dc_{m,2}}{dr} \tag{2.23}$$

The first two terms of Eq. (2.23), combine according to the differentiation product rule to yield Eq. (2.24).

$$\frac{1}{\rho}\frac{dp_{t,2}}{dr} = \frac{c_{\theta,2}}{r}\frac{d(rc_{\theta,2})}{dr} + c_{m,2}\frac{dc_{m,2}}{dr} \tag{2.24}$$

The left-hand side of Eq. (2.24), can be expressed in terms of the specific work done by an elemental-blade-cascade ($Y_{t,ca}$) according to Eq. (2.25). Here it is assumed that the circumferential velocity at rotor inlet is zero.

$$Y_{t,ca}(r) = \omega\eta_h r c_{\theta,2} \tag{2.25}$$

Differentiating Eq. (2.25) with respect to r yields Eq. (2.26).

$$\frac{dp_{t,2}}{dr} = \omega\eta_h\rho\frac{d(rc_{\theta,2})}{dr} \tag{2.26}$$

Combining Eq. (2.24) and Eq. (2.26), yields Eq. (2.27). Finally, for radial equilibrium to be achieved, i.e., for the streamlines to lie on co-axial cylindrical surfaces Eq. (2.27), needs to be satisfied by every elemental-blade-cascade along the rotor blade span. The term, $rc_{\theta,2}(r)$, is labeled as the swirl-distribution, and $Y_{t,ca}(r)$ as the blade-loading distribution. Both the swirl-distribution and blade-loading-distribution are functions of the blade radius (r).

$$\omega\eta_h\frac{d(rc_{\theta,2})}{dr} = \frac{c_{\theta,2}}{r}\frac{d(rc_{\theta,2})}{dr} + c_{m,2}\frac{dc_{m,2}}{dr} \tag{2.27}$$

2.6 Blade loading distribution

The swirl-distribution ($rc_{\theta,2}$) along the blade span is user-defined and dictates the corresponding unknown meridional velocity distribution at rotor exit, $c_{m,2}(r)$. To obtain the meridional velocity distribution, the specified swirl-distribution is

substituted into Eq. (2.27) and then subsequently integrated with respect to blade radius (r). Ultimately, determining the radial distribution of $c_{m,2}(r)$, and $c_{\theta,2}(r)$ allows for the calculation of the velocity triangles at rotor inlet and outlet.

Here it is assumed, the radial velocity at rotor inlet and rotor outlet is zero, i.e., the radial equilibrium boundary condition is satisfied. Additionally, it is assumed that the inlet is swirl free, i.e., $\overrightarrow{c_{\theta,1}} = 0$. The meridional velocity remains constant between rotor inlet and outlet, i.e., $\overrightarrow{c_{m,1}} = \overrightarrow{c_{m,2}}$.

There are typically two choices for the blade-loading-distribution: an iso-energetic loading distribution and radius dependent loading distribution.

2.6.1 Iso-energetic blade loading distribution

For an iso-energetic design, the swirl-distribution ($rc_{\theta,2}$), and the blade-loading-distribution ($Y_{t,ca}$) are constant along the blade span, according to Eq. (2.28), where, b, is a constant. Substituting the aforementioned swirl-distribution into Eq. (2.27) yields Eq. (2.29). Integrating, Eq. (2.29), with respect to blade radius, r, will yield Eq. (2.30), where k is the integration constant. For an iso-energetic design, the meridional velocity will be constant along the blade span. The circumferential velocity distribution along the rotor blade span, can be calculated according to Eq. (2.28).

$$rc_{\theta,2} = b \qquad Y_{t,ca} = \omega\eta_h b \tag{2.28}$$

$$c_{m,2}\frac{dc_{m,2}}{dr} = 0 \tag{2.29}$$

$$c_{m,2} = k \tag{2.30}$$

To achieve a constant value of swirl-distribution at rotor exit along the blade span for an iso-energetic design, the circumferential velocity component at the rotor hub has to be larger compared to at the tip, as radius of the hub is smaller than the tip, i.e, $c_{\theta,hub} > c_{\theta,tip}$. The higher circumferential velocity of the flow at the hub, is achieved through higher flow turning by twisting the blades by a larger stagger angle (γ in Fig. 2.8), at the hub compared to the tip. This increases the risk of flow separation at the hub and therefore increases the possibility of significant aerodynamic losses, and noise produced.

To address the problem of risk of flow separation at the hub, a radius dependent blade-loading-distribution is often implemented. This approach aims at utilizing higher blade spans more effectively and consequently off-loading the hub. Off-loading a blade section, refers to a reduced flow-turning at that particular blade section. This is typically achieved by reducing the stagger-angle at the specified blade section.

2.6.2 Radius dependent blade-loading-distribution

For a radius dependent blade-loading-distribution, the swirl-distribution is considered to be a function of the blade-radius. A linear blade-loading-distribution, can be

achieved by defining the swirl-distribution $rc_{\theta,2} = ar + b$, where a and b are non-zero constants. Substituting, the aforementioned swirl-distribution into Eq. (2.27) and integrating with respect to the blade radius, yields the radial distribution of meridional velocity , according to Eq. (2.32), where k is an integration constant. Increasing the value of a, increasingly off-loads the hub section and consequently increases the loading at higher blade-spans.

$$rc_{\theta,2} = (ar + b) \tag{2.31}$$

$$c_{m,2}(r) = \sqrt{2\left(\omega\eta_h ar - a^2 ln(r) + \frac{ab}{r}\right) + k} \tag{2.32}$$

A polynomial based swirl-distribution is also often implemented with the goal of off-loading the hub region, i.e., $rc_{\theta,2} = ar^{m+1} + b$, where a, and m, are user defined constants to vary the swirl-distribution at rotor exit. Following the same process of substituting the swirl-distribution into Eq. (2.27) and integrating with respect to the blade radius, yields the radial distribution of meridional velocity at rotor exit, according to Eq. (2.34), where k is an integration constant.

$$rc_{\theta,2} = \left(ar^{m+1} + b\right) \tag{2.33}$$

$$c_{m,2}(r) = \sqrt{2(m+1)\left[a\omega\eta_h \frac{r^{m+1}}{m+1} - \left(\frac{a^2 r^{2m}}{2m}\right) - \left(\frac{abr^{m-1}}{m-1}\right)\right] + k} \tag{2.34}$$

Both linear and polynomial blade-loading-distributions off-load the hub region. However, they consequently increase the specific work done at higher blade spans. This can negatively affect the flow near the rotor blade tip, leading to increased tip blockage and earlier onset of stall. To address these problems, a parabolic blade-loading-distribution can be used. This approach off-loads both the hub and the tip regions, concentrating maximum specific work at the mid-blade span. In this work, the parabolic blade-loading-distribution is defined with adjustable parameters. This allows precise control over the location of the peak blade loading point along the blade span.

A swirl-distribution, $rc_{\theta,2} = a(r-d)^2 + e$, is defined to obtain a parabolic blade-loading-distribution. The value of the constant d, can be changed to values between rotor hub diameter, and rotor tip diameter to allow for the location of the peak blade loading to be set to a desired position. Increasing the value of parameter a, allows for a sharper parabolic distribution. Again following, the same process of substituting the swirl-distribution into Eq. (2.27) and integrating with respect to the blade radius, yields the radial distribution of meridional velocity at rotor exit, according to Eq. (2.36), where k, and e are integration constants.

$$rc_{\theta,2} = \left(a(r-d)^2 + e\right) \tag{2.35}$$

$$c_{m,2}(r) = \sqrt{\begin{aligned} &2\Big((a\omega\eta_h - a^2)r^2 + (6a^2d - 2a\omega\eta_h d)r \\ &-(2ae + 6a^2d^2)\ln(r) - (2a^2d^3 + 2ade)\frac{1}{r}\Big) + k \end{aligned}} \tag{2.36}$$

The elemental volume flowrate (δQ_{ca}) can be calculated according to Eq. (2.37). The net volume flowrate through the entire fan blade annulus (Q_B) can then be obtained by summing the elemental volume flowrate over all elemental-blade-cascades from the rotor hub to the rotor tip according to Eq. (2.37). During the design process, the volumetric efficiency (η_{vol}) needs to be taken into account, i.e., the rotor blade should be designed for a volume flowrate greater than the target volume flowrate, i.e., $Q_{target} = Q_B/\eta_{vol}$.

$$\delta Q_{ca} = (2\pi c_{m,2} r)\,\delta r \qquad Q_B = 2\pi \int_{r_{hub}}^{r_{tip}} c_{m,2} r dr \tag{2.37}$$

The design blade power (P_B) is then calculated according to Eq. (2.38). The design specific blade energy (Y_B) and total-to-total pressure rise ($p_{tt,B}$) for the blade can be obtained using Eq. (2.39).

$$P_B = 2\pi\rho\omega \int_{r_{hub}}^{r_{tip}} c_{m,2} c_{\theta,2} r^2 dr \tag{2.38}$$

$$Y_B = \left(\frac{P_B}{\rho Q_B}\right) \qquad p_{tt,B} = \left(\frac{P_B}{Q_B}\right) \tag{2.39}$$

For an iso-energetic, linear, and polynomial blade-loading-distribution design, the value of constants b and k are decided in an iterative manner till Q_B and $p_{tt,B}$ agree with the input design parameters. Similarly for the parabolic blade-loading-distribution, the constants e and k are decided in an iterative manner. Once the radial distribution of the meridional and circumferential velocity at the rotor exit is determined, the remaining velocity components, angles of the inlet and outlet can be determined using aforementioned formulae.

A typical radial distribution of $c_{m,2}$, $c_{\theta,2}$, c_2 and $Y_{t,ca}$ for the different blade-loading-distributions is illustrated in Fig. 2.10. Identical Q_{target}, $p_{tt,B}$, blade count (z_b), fan diameter (d_{fan}), and hub-to-tip diameter ratio (κ) is used to obtain the radial distributions for the different blade-loading-distributions illustrated in Fig. 2.10. For the linear swirl-distribution, parameter, a, is set to a value of 3.0. For the polynomial swirl-distribution, parameters a and m are set to 12.0 and 2.0, respectively. For the parabolic swirl-distribution, parameters a and d are set to a value of 60.0 and 0.135, respectively. A value of 0.135 for d, corresponds to the blade mid-span, for this particular example. The corresponding integration constants are documented below.

- Linear swirl-distribution: b = 1.0 , k = -193.71
- Polynomial swirl-distribution: b = 1.39 , k = 115.43
- Parabolic swirl-distribution: e = 1.47, k = -2096.92

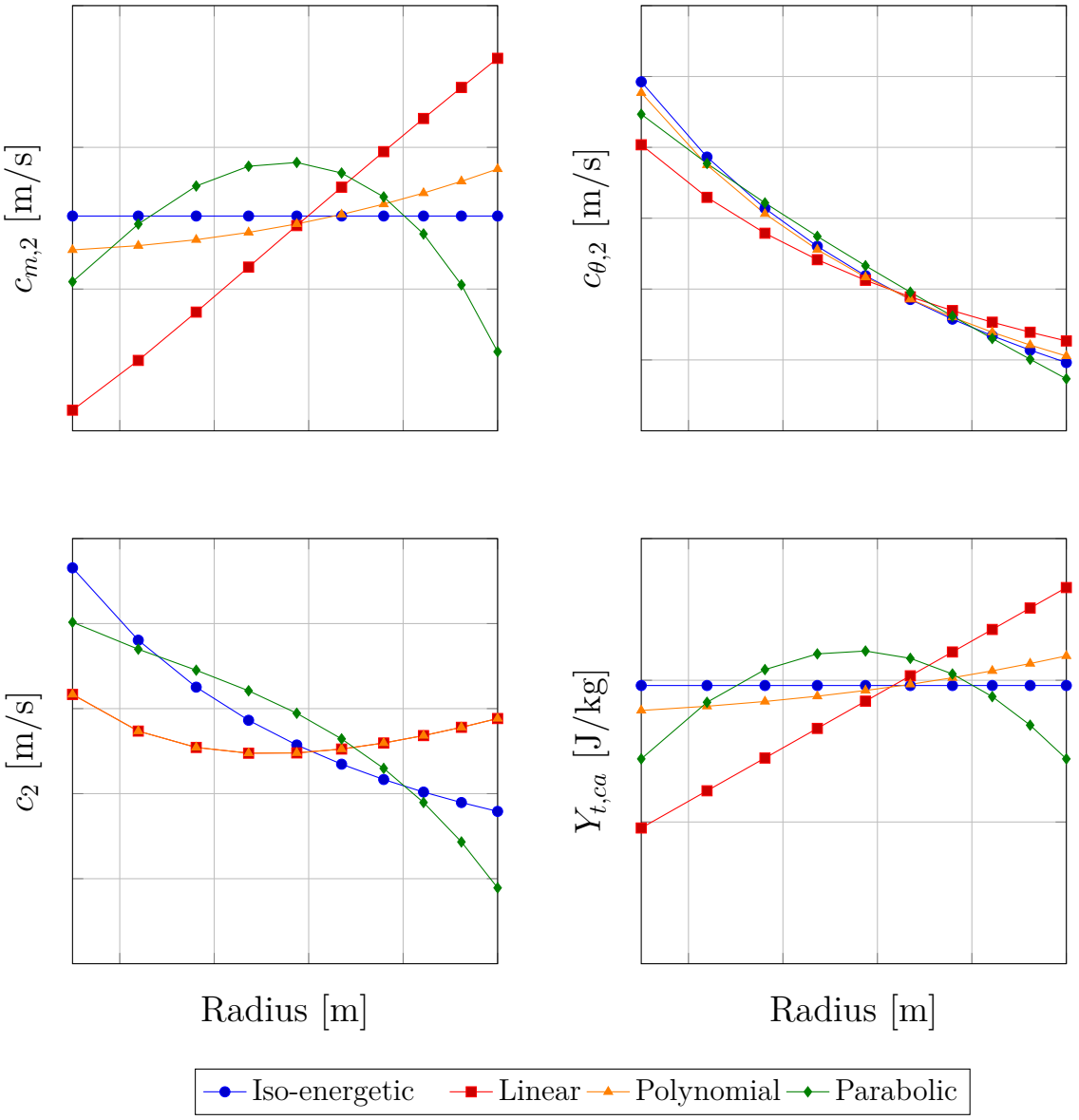

Figure 2.10: Radial distribution of $c_{m,2}$, $c_{\theta,2}$, c_2, and $Y_{t,ca}$ for different swirl distributions

2.7 Weakly cambered airfoil profile

Typically low-pressure axial fans have a low-blade count (z_b), high-circumferential blade spacing (s_b), and consequently have low-solidity blades [44, 47–49, 58]. Blade solidity is defined as the ratio of blade chord-length (l_c) to the blade spacing (s_b), according to Eq. (2.40). For low-pressure axial fans the blade solidity should be maintained below 0.7 for all considered elemental-blade-cascades, to ensure limited aerodynamic interaction from adjacent blades [38, 44].

$$\sigma = \left(\frac{l_c}{s_b}\right) \tag{2.40}$$

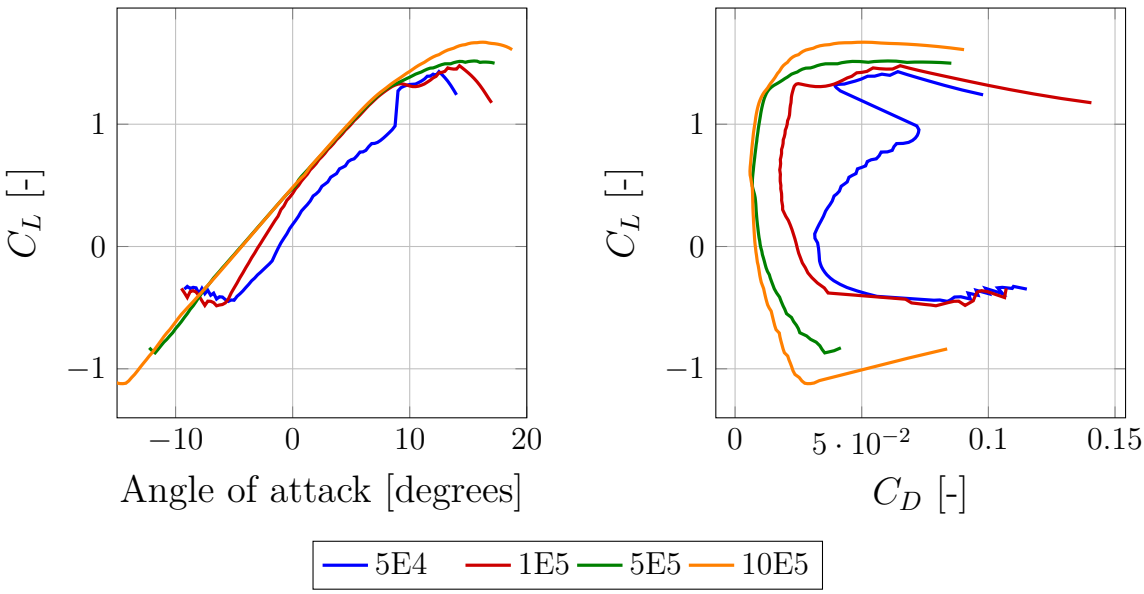

Figure 2.11: Polar curves for the NACA 4412 isolated airfoil at different Reynolds number: C_L vs α (**left**) and C_L vs C_D (**right**).

The four digit National Advisory Committee for Aeronautics (NACA) [59] airfoil series is a common choice for low-pressure axial fan blade design since these airfoil profiles allow for the individual control of the mean camber line and the thickness distribution around the same. This series of airfoils generate weakly cambered blades ($f/l_c < 0.1$), where, f, is the maximum camber. The first digit of a four digit NACA airfoil indicates the maximum camber as a percentage of the chord length. The second digit indicates the position of the maximum camber as a percentage of chord length. The last two digits indicate the maximum thickness as a percentage of the chord length.

The choice of airfoil provides the airfoil polar curves, i.e., the lift coefficient (C_L) and the drag-to-lift ratio ($\varepsilon = C_D/C_L$) as a function of the angle of attack (α) and Reynolds Number (Re). The airfoil polar curves for an isolated NACA 4412 airfoil is illustrated in Fig. 2.11, for a range of Re numbers. The airfoil polar curves can be computed with the public domain code XFOIL by Drela [60].

It is observed that as Reynolds number increases the the lift coefficient curve converges. Similarly, the lift-to-drag ratio curves converge with increased Reynolds number. Typically it is recommended that the Reynolds number calculated using the blade chord length (l_c) as the reference dimension, be maintained above $1.5 * 10^5$ for all blade segments [38]. This is however, difficult to achieve for small-diameter fans which rotate at slow speeds.

The choice of angle of attack dictates the rotor geometry. Three options exist for the choice of angle of attack. The first option is to choose the angle of attack (α) such that the peak lift coefficient (C_L) is achieved. This leads to the lowest solidity blades, with maximum blade spacing but comes with the disadvantage that the BEP lies close to the stall point and therefore part-load operation becomes challenging. The second option is to choose the angle of attack (α) such that the minimum drag-to-lift ratio

(ε) is achieved which yields blades with maximum hydraulic efficiency. Alternatively, a compromise between the two previous choice may be made.

As an example, from the airfoil polar curves illustrated in Fig. 2.11, for the isolated NACA 4412 airfoil at $Re = 2 * 10^5$, the peak lift coefficient (C_L) of 1.44 is obtained for an angle of attack (α) equal to 15.3°. Similarly, the minimum drag-to-lift ratio (ε) of 0.012 is obtained for an angle of attack of 7°. Either 15.3°, 7°, or an value between the two may be used as the angle of attack of choice for elemental-blade-cascades at different blade radius.

2.8 Blade element momentum method

The key equation for the Blade Element Momentum (BEM) method links the blade solidity (σ) to the specific work done by the elemental-blade-cascade ($Y_{t,ca}$), the velocity triangles, and the aerodynamic airfoil parameters, according to Eq. (2.41). In Eq. (2.41), w_∞ is the vectorial mean of the relative inlet velocity (w_1) and relative outlet velocity (w_2). The magnitude of w_∞ is calculated according to Eq. (2.43) [38, 43].

$$\sigma = \frac{2\, Y_{t,ca}}{\omega r w_\infty\, C_L \left(1 + \frac{\varepsilon}{tan\beta_\infty}\right)} \tag{2.41}$$

$$\overrightarrow{w}_\infty = \frac{1}{2}\left(\overrightarrow{w}_1 + \overrightarrow{w}_2\right) \tag{2.42}$$

$$w_\infty = \frac{1}{2}\sqrt{\left(u + \sqrt{w_2^2 - c_m^2}\right)^2 + 4c_m^2} \tag{2.43}$$

The blade spacing (s_b) and the chord length (l_c) is calculated, according to Eq. (2.44) using an assumed blade count (z_b).

$$s_b = \left(\frac{2\pi r}{z_b}\right) \qquad l_c = \sigma s_b \tag{2.44}$$

Once the blade chord length is determined the twist of the blade along the blade span needs to be calculated, i.e., the stagger angle (γ in Fig. 2.8) for each individual blade segments can be determined. The stagger angle of each blade segment is calculated as the sum of the angle of attack (α) and the vectorial mean flow angle (β_∞) [38, 43].

$$\beta_\infty = tan^{-1}\left(\frac{2c_m}{u + \sqrt{w_2^2 - c_m^2}}\right) \tag{2.45}$$

$$\gamma = \beta_\infty + \alpha \tag{2.46}$$

A typical radial distribution of the blade solidity (σ), chord length (l_c), blade spacing (s_b), and stagger angle (γ) using a NACA 3510 airfoil profile and minimum

drag-to-lift ratio (ε) as the choice for angle of attack, is illustrated in Fig. 2.12 for the different swirl distributions described in Sec. 2.6. The solidity, chord length, and stagger angle at all blade sections are dependent on the choice of swirl distribution. The blade spacing is only dependent on the choice of blade count (z_b). Linear, polynomial and parabolic swirl distribution enable for the stagger angle at the rotor hub to be reduced compared to the iso-energetic design. The linear swirl distribution generates the least blade stagger angle at the hub. Alternatively, the linear and polynomial swirl distributions produce blade designs with maximum stagger angle at the rotor tip. The iso-energetic swirl distribution yields designs with maximum chord length at the hub. Note, that the blade chord length, solidity, and stagger angle can all be altered by changing the input design parameters, and the corresponding integration constants.

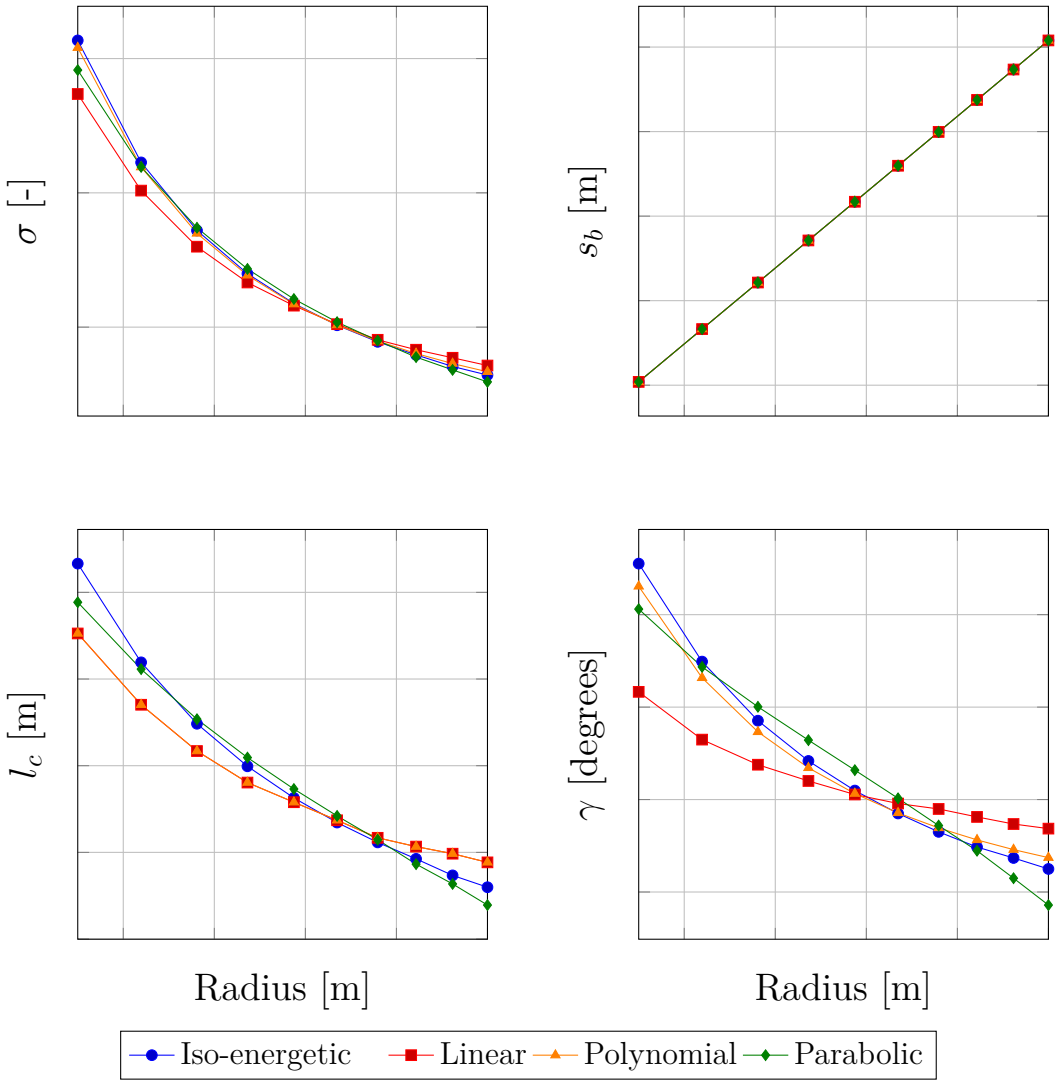

Figure 2.12: Radial distribution of σ, s_b, l_c, and γ for different swirl distributions

Chapter 3

Low Pressure Axial Fans - Aeroacoustics

Sound waves are small perturbations in pressure and density that propagate through the fluid medium in the form of longitudinal waves. These sound waves are generated by turbulent eddies convected by the mean flow coming in contact with a solid body, which generates a rapid pressure change on the surface of the solid body. These rapid pressure changes propagate through the medium as sound waves.

The frequency of the fluctuations which results from this interaction between the turbulent eddies and the solid body are determined by the eddy size (L in m) and their convection velocity (U_c in m/s), calculated according to Eq. (3.1). The size of the eddies are usually in the same order of magnitude as the smallest dimension of the mean flow. The sound waves generated at this frequency will correspondingly have a wavelength (λ in m), calculated according to Eq. (3.1), where, c_o, is the speed at which the the sound waves propagate through the medium.

$$f = \left(\frac{U_c}{L}\right) \qquad \lambda = \left(\frac{Lc_o}{U_c}\right) \qquad c_o = \sqrt{\gamma RT} \tag{3.1}$$

The pressure at any point in the flow is a function of both the position and time and is calculated as the sum of the ambient pressure (p_∞ in Pa) and a time varying pressure perturbation ($p^{'}(t)$). The time varying pressure perturbation is calculated according to Eq. (3.2).

$$p^{'}(t) = (p(t) - p_\infty) \tag{3.2}$$

The human ear is able to perceive sound waves between a frequency range of 20 Hz to 20 kHz. The lower threshold of hearing is at $p^{'}_{rms}$ of $20\mu Pa$, which is barely perceivable sound at a frequency of 1 kHz. The upper threshold of hearing is at $p^{'}_{rms}$ of $20Pa$, at a frequency of 1 kHz. The human ear's sensitivity is logarithmic and is measured using a decibel scale, referred to as the sound pressure level (SPL) and is calculated according to Eq. (3.3), in terms of the root mean square of the fluctuating pressure time history (p_{rms}) and a reference pressure (p_{ref}). For almost all airborne applications the standard $p_{\text{ref}} = 20\mu\text{Pa}$. Subsequently, p_{rms} is the time average of the square of the fluctuating pressure and calculated according to Eq. (3.4)

$$\mathrm{SPL} = 20\log_{10}\left(\frac{p_{\mathrm{rms}}}{p_{\mathrm{ref}}}\right) \tag{3.3}$$

$$p_{rms} = \sqrt{\frac{1}{2T}\int_{-T}^{T}(p(t) - p_{\mathrm{o}})dt} \tag{3.4}$$

3.1 Airfoil noise generation mechanisms

Airfoil noise generation mechanisms can be broadly classified into airfoil self-noise components and interaction noise. Depending on the noise mechanism, the characteristics and the part of the acoustic spectrum affected changes.

3.1.1 Airfoil self noise

The noise that an airfoil generates when it is subjected to spatially uniform and non-turbulent flow is labeled as airfoil self-noise. Airfoil self-noise can be further classified into turbulent boundary layer noise, boundary layer separation noise, trailing edge noise, and tip noise. Each of the aforementioned noise generation mechanisms have different characteristics and consequently affect different parts of the acoustic spectrum.

Boundary Layer Noise

Turbulent boundary layer noise is a broadband noise source generated as a result of the airfoil surface interacting with the pressure fluctuations in the turbulent boundary layer. Turbulent boundary layer noise marks the lower limit of the broadband spectrum [61–64].

Boundary Layer Separation Noise

Boundary layer separation noise is generated when the airfoil operates in deep stall conditions, and large scale flow separations exist on the surface of the airfoil. Stall occurs when the airfoil section is subjected to a high incidence angle, which in turn leads to a flow separation near the Leading Edge (LE) of the airfoil. Boundary layer separation noise has broadband noise characteristics. If an airfoil operates in stall conditions, boundary layer separation noise is considered to be the dominant noise source and can mask tonal noise components [61–64].

Trailing Edge Noise

Trailing Edge (TE) noise is generated as a result of the vortex shedding past the TE of an airfoil. The characteristic of the noise generated depends both on the shape of the TE (sharp/blunt), and the boundary layer properties (laminar/turbulent) [61–64]. Laminar TE noise, is generated when a laminar boundary layer is formed on at least one side of the airfoil and the vortices are convected past the TE. The

noise generated is tonal and is observed to appear at frequencies identical to the vortex shedding frequency in the acoustic spectrum.

In a turbulent boundary layer, eddies are convected past the TE. The vorticity and shedding frequency depend on the boundary layer properties and TE shape. The emitted sound has high frequency broadband characteristics. However, a sharp trailing edge acts as an efficient tonal noise source. A blunt trailing edge causes vortex shedding, similar to a Karman vortex street, in both laminar and turbulent flows. This produces dipole tonal noise. The shedding frequency increases as the TE thickness decreases.

Tip Noise

Tip noise exists for any geometry with an open ended airfoil cross-section. Secondary flow structures, commonly referred to as tip vortices are formed as a result of the pressure difference between the pressure and suction side of the airfoil. The strength of the tip vortices is also strongly dependent on the pressure difference between the pressure and suction side of the airfoil. Tip vortex formation is exacerbated by high incidence angles, and by the geometry of the tip. The inherently unsteady pressure fluctuations generated as a result of the tip vortex lead to the generation of tip noise. Tip noise has broadband characteristics and affects the mid-frequency region of the acoustic spectrum [65–69]. Tip noise can be a significant noise source, when the tip vortex interacts with surrounding walls, in cases such as a ducted fan.

3.1.2 Interaction noise

Additional noise generation mechanisms are introduced as a result of the airfoil interacting with turbulent and spatially non-uniform flow. Depending on the length scale of the turbulent structures (Λ) interacting with the airfoil, different parts of the acoustic spectrum are affected. The integral length scale, is the measure of the largest turbulent structures in the energy spectrum.

If the incident turbulence has length scales significantly larger than the airfoil chord length ($\Lambda >> l_c$), the airfoil loading fluctuates, i.e., the lift and drag forces generated by the airfoil are unsteady. The radiated sound has wavelength (λ) significantly larger than the blade chord length, and therefore the airfoil is considered to be acoustically compact, and the generated sound cannot be assigned to a specific part of the airfoil. The generated noise is assigned to the low-frequency broadband part of the acoustic spectrum [38, 61, 63].

If the incident turbulence has length scales comparable to that of the airfoil chord length ($\Lambda \leq l_c$), the airfoil can no longer be considered acoustically compact, and the sound produced is attributed to the airfoil leading edge (LE). The noise generated is still of broadband nature, but assigned to a higher frequency range of the acoustic spectrum compared to the case where, $\Lambda >> l_c$.

Typically the low frequency part of the acoustic spectrum is dominated by turbulence ingestion noise, while the higher frequency part of the acoustic spectrum is dominated by the airfoil self-noise.

3.2 Rotor noise generation mechanisms

Similar to airfoil self-noise, the noise produced by the rotor when ingesting spatially homogeneous, non-turbulent flow is labeled as rotor self-noise. In addition to the airfoil self-noise generation mechanisms, as a result of the rotational motion of the rotor, additional self noise components are introduced. In particular, blade thickness noise, steady loading noise, subharmonic tip noise, are the additional noise generation mechanisms which arise as a result of the rotational motion of the rotor.

Blade thickness noise

Blade thickness noise is generated as a result of the volume displacement of fluid as a result of the rotational motion of the rotor, leading to periodic pressure fluctuations in the adjacent flow-field. The frequency of these periodic pressure fluctuations is equal to the shaft rotational frequency ($f_{SF} = 1/n$ in Hz) and has tonal characteristics. However, for low-pressure fans which typically have low circumferential velocities at the rotor tip compared to the speed of sound, i.e., low subsonic tip Mach numbers ($Ma < 0.3$), the radiation efficiency of these pressure fluctuations are considered to be weak and are therefore commonly disregarded for low-pressure fans [62, 70].

Steady loading noise

A rotor operating in a spatially uniform flow field will experience steady blade forces. This force is steady to an observer in the rotational frame of reference, i.e., moving with the rotor. The sound produced as a result of the rotor blade interacting with the flow-field will not be audible to an observer in the rotational frame of reference. However, an observer in the stationary frame of reference experiences harmonic pressure changes, induced by the rotating pressure field. The sound produced has tonal characteristics and is observed at the blade passing frequency ($f_{BPF} = nz_b$). Steady loading noise, is often referred to as Gutin noise and is a dipole noise source. Like blade thickness noise, due to the low tip Mach numbers for low-pressure fans, Gutin noise contributes minimally to the overall sound emission for low-pressure fans [62, 71].

Subharmonic tip noise

As a result of the rotor's rotational motion, an additional noise component called subharmonic tip noise is introduced [72–75]. This noise generation mechanism occurs when the fan operates at low flow coefficients (φ). At low flow-coefficients, the meridional velocity component is low, while the circumferential velocity component near the tip region is high due to end-wall effects in ducted fans. As a result, the inlet swirl angle at the rotor tip increases substantially compared to other blade spans. A large inlet swirl angle leads to large angles of incidence, promoting the formation of tip vortices. Some of these vortices are convected downstream by the mean flow through the annular tip gap. However, coherent tip structures, which rotate circumferentially with the rotor, are also formed. These structures rotate

at an angular velocity lower than that of the rotor, causing them to interact with adjacent blades. Subharmonic tip noise appears as a narrowband hump in the acoustic spectrum at frequencies different from the blade passing frequency (BPF). The first harmonic of this noise typically occurs at frequencies lower than the BPF ($f < f_{BPF}$), and can often be a dominant noise source in low-pressure axial fans at low flow-coefficients.

Unsteady loading noise

A rotor ingesting a spatially non-uniform and steady flow field will experience unsteady blade forces. The unsteady of the blade force is a result of the magnitude and the swirl of the incoming flow depending on the angular position of the rotor blade. Similar to the steady blade loading noise, an observer in the stationary frame of reference experiences harmonic pressure changes induced by the rotating unsteady pressure fields. The generated noise has tonal characteristics observed at the BPF and harmonics. Rotor-stator interactions are a prominent source of unsteady loading noise.

Rotating stall noise

Rotating stall is a phenomenon which occurs when a fan is operated at low flow-coefficients and an arbitrary local disturbance stalls the flow in one of the blade passages, i.e., area between the suction side of one blade and the pressure side of the adjacent blade. Stall leads to the marked decrease in the massflow through the blade passage by partially blocking the blade passage. As a result of a particular blade passage being blocked, the flow is deflected towards the adjacent blade passage. The flow being re-directed to adjacent blade passage, leads to the originally stalled blade passage to correct itself and un-stall itself. This process repeats itself, and the stalled blade passage moves circumferentially from one blade passage to the next at approximately 30% to 50% of the shaft rotational frequency, in a direction opposite to the rotational direction of the rotor [62, 76]. The resulting unsteady blade forces lead to the generation of a narrowband noise which is emitted at $f \approx 0.7 f_{BPF}$ and higher harmonics.

Turbulence ingestion noise

Similar to airfoils ingesting turbulent flow, the low frequency broadband region of the acoustic spectrum is expected to be affected as a result of a rotor ingesting turbulent flow [77–80]. The summary of the different noise generation mechanisms for a rotor is summarized in Tab. 3.1 and illustrated in Fig. 3.1. Typically rotor self noise affects the high frequency region of the acoustic spectra, while turbulence ingestion is expected to have an effect on the low frequency region of the acoustic spectra. Wright [63] incorporated the contributions of the different aeroacoustic sound sources for axial fans into a schematic acoustic spectrum [63], and Krömer [43], further extended upon it.

Table 3.1: Classification of rotor noise mechanisms

Noise Mechanism	Tonal	Narrowband	Broadband
Boundary layer noise			■
Boundary layer separation noise	■		■
Trailing edge noise (laminar BL)	■		
Trailing edge noise (turbulent BL)			■
Tip noise			■
Subharmonic tip noise		■	
Blade thickness noise	■		
Steady loading noise	■		
Unsteady loading noise	■		
Rotating stall noise		■	
Turbulence ingestion noise			■

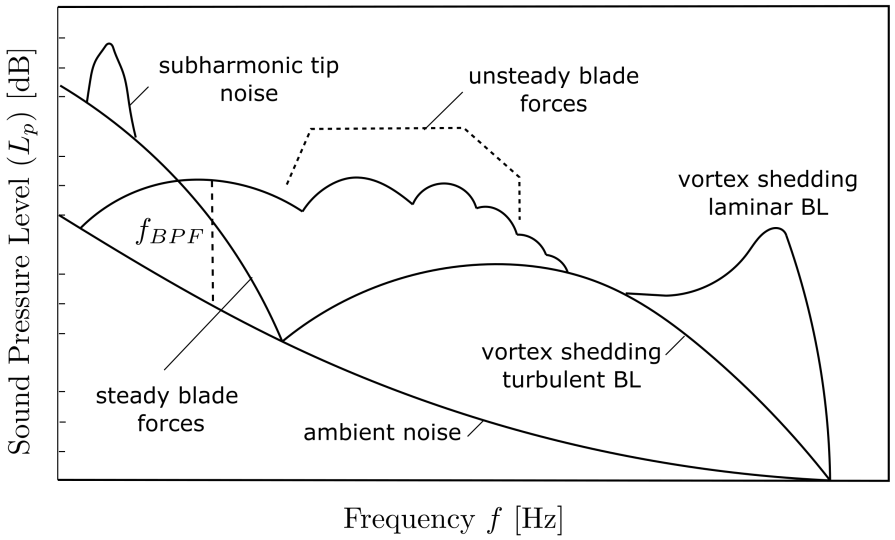

Figure 3.1: Schematic acoustic spectrum of an axial fan, adapted from [43, 63].

3.3 Hybrid Computational Aeroacoustics

Aero-acoustic solvers aim to find this time varying pressure perturbation ($p^{'}(t)$), to subsequently calculate the acoustic far-field. There are two main approaches in Computational Aero-Acoustics (CAA).

1. **Direct Approach**: A transient solution is obtained by solving the compressible Navier-Stokes equations directly using Direct Numerical Simulation (DNS) or Large Eddy Simulation (LES) to obtain the far-field pressure perturbations, i.e., the spatial and the temporal resolution of the computational grid must be sufficiently fine to capture acoustic waves with the highest desired

frequency. Additionally, the computational grid must include the far-field observers. Consequently, significant computational resources are necessary.

2. **Hybrid Approach**: Hybrid methods assume one-way coupling between the hydrodynamic flow field and acoustic field, i.e., the flow-field is assumed to be independent of the acoustic field. This assumption is valid for most low-mach and super-sonic applications but fails to be true in the hyper-sonic regime or regimes with large density variations. This approach allows for the problem to be divided into two parts, with one being the solution to the hydrodynamic and acoustic near-field and other, the propagation of sound waves. Therefore only the sound source needs to be simulated and different analogies can then be implemented to propagate the acoustic waves to the far field. In the appended papers, a hybrid computational aero-acoustic approach is used for predicting the far-field sound.

3.3.1 Ffowcs Williams and Hawkings Analogy

The Ffowcs Williams and Hawkings (FWH) analogy equation is an exact rearrangement of the continuity equation and the Navier-Stokes equations into the form of an inhomogeneous wave equation with two surface source terms (monopole and dipole) and a volume source term (quadrupole). The FWH analogy ultimately provides the far-field acoustic pressure fluctuation ($p^{'}$), given an accurate numerical calculation of the pressure fluctuation on a surface which bounds the source region. The most useful applications of the FWH analogy is in the calculation of the acoustic far field from detailed numerical simulations of a flow within a limited region containing the source region. The FWH surface may be arbitrarily located within the numerical domain, in a region where there is high confidence in the calculations.

The FWH analogy computes the far field acoustic pressure perturbation p' at any point outside the region of turbulence as function of time according to Eq. (3.5). Source term 1, 2, and 3 on the right hand side of Eq. (3.5) refer to the quadrupole, dipole, and monopole terms respectively.

The thickness noise (monopole source) is determined by the geometry and kinematics of the body. The loading noise (dipole source) is generated by the force that acts on the fluid as a result of the presence of the body. The quadrupole source term accounts for nonlinear effects, such as nonlinear wave propagation, variations in the local sound speed, and noise generated by shocks, vorticity and turbulence in the flow field. The source terms are inter-dependent but the separation in their physical interpretation allows for some flexibility depending upon the physics of the problem. For a low speed flow the quadrupole source term can be neglected, similarly in the rotor plane only the thickness term (monopole source) is dominant and the other two source terms may be neglected. The main disadvantage of the traditional FWH approach is that to predict noise produced by a body operating in the transonic regime, the quadrupole source terms has to be included. The quadrupole source term is a volume source term and therefore a volume integration has to be performed over the entire source region, which is computationally expensive.

$$\Box^2 p^{'}(\vec{x},t) = Quadrupole + Dipole + Monopole \tag{3.5}$$

$$Quadrupole = \frac{\partial^2}{\partial x_i \partial x_j} T_{ij} H(f) \tag{3.6}$$

$$Dipole = -\frac{\partial}{\partial x_i}[P_{ij}\hat{n_j} + \rho u_i(u_n - v_n)\delta(f)] \tag{3.7}$$

$$Monopole = \frac{\partial}{\partial t}[\rho_o v_n + \rho(u_n - v_n)\delta(f)] \tag{3.8}$$

$$\Box^2 = \frac{1}{c^2}\frac{\partial^2}{\partial t^2} - \nabla^2 \tag{3.9}$$

$$T_{ij} = \rho u_i u_j + (p' - c_o^2 \rho')\delta_{ij} - \tau_{ij} \tag{3.10}$$

3.3.2 Farassat 1A Formulation

The Farassat 1A Formulation [81] [82] provides an integral representation of the FWH equation, which does not take into consideration the quadrupole term (the volume source term) in Eq. (3.5). This assumption is valid when the flow is not in the transonic regime, i.e., valid for numerical simulations of low-speed axial fans.

Ω is the volume containing the moving surface. $\partial\Omega$ is the bounding FWH surface. $\vec{y}$ is the position of the far-field observer. $\vec{x}$ the position of the source at the point of integration on surface element. $\vec{r}$ is the distance between the observer and the source along the direction of radiation and is calculated according to Eq. 3.11. $\vec{n}$ is the outward facing normal to the FWH surface at the given point of integration. $\vec{v}$ is the velocity with which the solid body moves. Additionally all terms placed in square brackets are evaluated at retarded time, i.e., with respect to the source Eq. 3.12, where τ is the source time and t is the observer time. M is the local Mach number vector of the source. The subscripts n, r depict the components of the respective vectors in the FWH surface normal direction and the radiation direction respectively. The summation of the $p_T^{'}$ and the $p_L^{'}$ term yields the total pressure fluctuation terms as a function of time.

Implementing these equations in a CFD code involves the computing $p_T^{'}$ and the $p_L^{'}$ terms for each mesh face constituting the FWH surface and summing them over to obtain the total contribution of the FWH surface and then finally repeating the same procedure for all FWH surfaces.

$$\vec{r} = \vec{x} - \vec{y} \tag{3.11}$$

$$\tau = t - r/c \tag{3.12}$$

$$p'(\vec{x},t) = p'_T(\vec{x},t) + p'_L(\vec{x},t) \tag{3.13}$$

$$U_i = \left(1 - \frac{\rho}{\rho_o}\right) v_i + \frac{\rho u_i}{\rho_o} \tag{3.14}$$

$$L_i = P_{ij}\vec{n_j} + \rho u_i(u_n + v_n) \tag{3.15}$$

$$\begin{aligned} 4\pi p'_T(\vec{x},t) = \int_{f=0} \left[\frac{\rho_0(\dot{U}_n + U_{\dot{n}})}{r(1-M_r)^2}\right]_{ret} \\ + \left[\frac{\rho_0 U_n\Big(r\dot{M}_r + c_0(M_r - M^2)\Big)}{r^2(1-M_r)^3}\right]_{ret} d\Omega \end{aligned} \tag{3.16}$$

$$\begin{aligned} p'_L(\vec{x},t) = \frac{1}{4\pi c_0}\int_{f=0} \left[\frac{\dot{L}_r}{r(1-M_r)^2}\right]_{ret} + c_0\left[\frac{L_r - L_M}{r^2(1-M_r)^2}\right]_{ret} \\ + \left[\frac{L_r(r\dot{M}_r + c_0(M_r - M^2))}{r^2(1-M_r)^3}\right]_{ret} d\Omega \end{aligned} \tag{3.17}$$

Chapter 4

Fan Design

This chapter uses the BEM method from Ch.2 to design four fans. The key difference between the four fans are their respective blade-loading distribution. The four designs have iso-energetic, linear, polynomial, and parabolic blade-loading distributions. The framework for the in-house Python library, *C-Fan*, which is used to design the rotor geometry is also summarized in this chapter.

4.1 Input Design Parameters

The first step in the fan-design process is to define the input design parameters. The input design parameters, tabulated in Tab. 4.1 are used to design the series of low-pressure axial fans. These parameters are chosen in-line with a current generation of cooling-fans being used in several in-service vehicles. The fan diameter chosen here, enable them to be used in a multi-fan parallel setup. For the specified choice of input design parameters, the Mach number at the rotor tip is 0.165, according to Eq. (2.3), i.e., that the fan operates in the incompressible flow regime. The design process considers the flow to be incompressible (ρ_∞ = constant) everywhere within the blade passage. This is a valid assumption given the choice of fan diameter and rotational speed, and the corresponding tip Mach number of 0.165 ($Ma_{tip} < 0.3$). Additionally, the flow around a rotor blade is considered to be not influenced by adjacent blades.

Based on the input design parameters in Tab. 4.1, the specific-speed (σ) and specific-diameter (δ) are calculated as 0.97 and 1.95, respectively, which align well with the requirements outlined by Cordier for the use of an axial turbomachine.

In addition to the aforementioned, design parameters, an initial choice needs to be made for the blade count (z_b), and hub-diameter (d_{hub}). Low-pressure axial fans have low-solidity blading, i.e., low blade count and high circumferential blade spacing. Additionally, since these fans are mostly operational at low-vehicle speeds and act as flow-blockage at high vehicle speeds to downstream components, it is beneficial to design fans with small hub diameters.

For all four designed fans, the blade count is selected to be seven ($z_b = 7$), and a hub diameter of 90 mm is selected. This leads to a hub-to-tip diameter ratio (κ) of 0.50. The choice of blade count and hub diameter is verified later in the design

process. Additionally, typical values of hydraulic efficiency (η_h), and volumetric efficiency of (η_{vol}) of 90% and 95%, are respectively chosen. The assumed input design parameters are tabulated in Tab. 4.2.

Table 4.1: Input fan design parameters

Design Parameters	Value
Volume flow rate $[Q]$	0.80 m^3/s
Total-to-total pressure $[p_{tt}]$	500 Pa
Rotational speed $[\omega]$	3200 rpm
Fan Diameter $[d_{fan}]$	360 mm
Ambient Pressure $[P_\infty]$	101325 Pa
Ambient Temperature $[T_\infty]$	293 K

Table 4.2: Additional input design parameters

Design Parameters	Value
Blade count $[z_b]$	7
Hub Diameter $[d_{hub}]$	90 mm
Volumetric Efficiency $[\eta_{vol}]$	95 %
Hydraulic Efficiency $[\eta_h]$	90 %

4.2 Blade Segmentation

The second step of the rotor blade design process involves the segmentation of the blade annulus into elemental-blade-cascades. The segmentation of the blade annulus is done such that the through-flow area between successive co-axial cylindrical surfaces are equal (δA), as illustrated in Fig. 4.1. The radius of each elemental-blade-cascade is calculated according to Eq. (4.1). Here, r_{tip} and r_{hub} are the radius of the rotor hub and tip respectively and n is the number of elemental-blade-cascades which will be designed during the design process. The first and last elemental-blade-cascades will always coincide with the rotor hub and tip, respectively. The hub radius (r_{hub}) is assumed such that the hub-to-tip diameter ratio ($\kappa = 0.50$). All blade designs presented in this work, have been obtained by segmenting the through-flow area into ten elemental-blade-cascades ($n = 10$).

The corresponding through-flow area of the elemental-blade-cascades (δA) are calculated according to Eq. (4.2) and Eq. (4.3). The radial extension of the elemental-blade-cascades (δr) are calculated according to Eq. (4.4)

$$r_j = \sqrt{r_{hub}^2 + \frac{(j-1)(r_{tip}^2 - r_{hub}^2)}{n-1}} \tag{4.1}$$

$$\delta A_j = \left\{ \frac{\pi \left(r_{tip}^2 - r_{hub}^2 \right)}{n-1} \right\}; \qquad j = 2, ..., n-1 \tag{4.2}$$

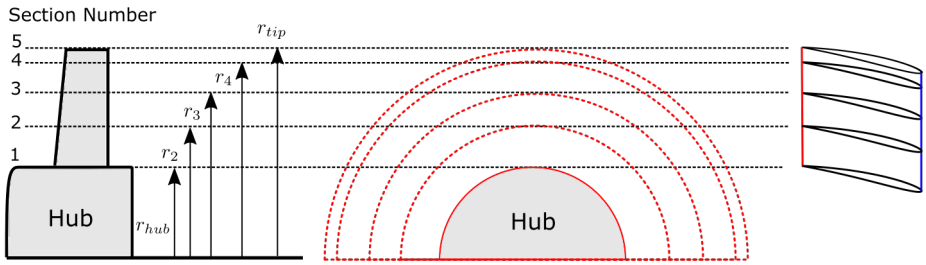

Figure 4.1: Segmentation of the blade annulus from rotor hub to tip, with equal area sections,adapted from [38]

$$\delta A_j = \left\{ 0.5 \frac{\pi \left(r_{tip}^2 - r_{hub}^2 \right)}{n-1} \right\}; \qquad j = 1, n \tag{4.3}$$

$$\delta r_j = \left\{ \frac{\delta A_j}{2\pi r_j} \right\} \tag{4.4}$$

4.3 Velocity Triangle Calculation

The next step in the design process, is to decide the blade-loading distribution parameters. In this work, four different blade-loading-distributions are considered: iso-energetic, linear, polynomial, and parabolic.

For linear blade-loading-distribution, the value of parameter a is user-defined. For polynomial blade-loading-distribution, the value of parameters, a and m are user-defined. For parabolic blade-loading-distribution, the values of parameters a and d are user defined. The values chosen for each of the parameters is tabulated in Tab. 4.3. These values may be changed to obtain different blade-loading distributions along the rotor blade span.

Table 4.3: Blade loading constants

Blade-Loading-Distribution	Swirl Distribtuion	Parameter Value
Iso-energetic	$rc_{\theta,2} = \text{b}$	-
Linear	$rc_{\theta,2} = ar + b$	a = 5.0
Polynomial	$rc_{\theta,2} = ar^{m+1} + b$	a = 12, m = 3
Parabolic	$rc_{\theta,2} = a(r-d)^2 + e$	a = -80, d = 0.135

For the chosen values of input parameters, the meridional velocity ($c_{m,2}$), is calculated for each individual elemental-blade-cascade along the blade span. For linear blade-loading-distribution, $c_{m,2}$ and $c_{\theta,2}$ at the rotor exit for the ten ($n = 10$) individual elemental-blade-cascades along the blade span is calculated according to Eq. (2.31) and Eq. (2.32), respectively. For polynomial blade loading, the meridional

and circumferential velocity at the rotor exit for individual elemental-blade-cascades are calculated according to Eq. (2.33) and Eq. (2.34), respectively. For polynomial blade loading, the meridional and circumferential velocity at the rotor exit for individual elemental-blade-cascades are calculated according to Eq. (2.35) and Eq. (2.36), respectively. However, the equations for calculating the meridional and circumferential velocity components at the rotor exit, contain a pair of unknown constants, b and k or e and k.

To be able to determine the values of $c_{m,2}$ and $c_{\theta,2}$, an iterative process is followed. First, an initial value of the unknown constants are assumed and the corresponding value of the $c_{m,2}$ and $c_{\theta,2}$ are calculated for every elemental-blade-cascade along the blade span. The corresponding net volume flowrate (Q_B), and the total-to-total pressure rise ($p_{tt,B}$) are then calculated according to Eq. (2.37) and Eq. (2.38), respectively.

The values of the unknown constants need to be iterated till the calculated value of Q_B, and $p_{tt,B}$ agree well with the input design parameters. For this work, it is ensured that the value of the unknown constants are chosen such that the calculated value of Q_B is within 0.1 % of the target volume flowrate, i.e., 0.842 m^3/s (Q/η_{vol}). Similarly, it is ensured that the calculated $p_{tt,B}$ is within 0.1 % of the target total-to-total pressure rise, i.e., 500 Pa. The values of the integration constants for the four different blade loading designs are tabulated in Tab. 4.4.

Table 4.4: Integration constants

Blade-Loading-Distribution	Parameter Value	Unknown Constants
Iso-energetic	-	b = 1.430, k = 140.69
Linear	a = 5	b = 0.689, k = -407.4
Polynomial	a = 12, m = 3	b = 1.420, k = 138.82
Parabolic	a = -80, d = 0.135	e = 1.47, k = -3955.7

Once $c_{m,2}$, and $c_{\theta,2}$ are calculated using the final values of the integration constants for all ten elemental-blade-cascades along the rotor blade span, the remaining components of the velocity triangles can be calculated, i.e., $w_{1,2,\infty}$, $\alpha_{1,2}$, $\beta_{1,2,\infty}$, $c_{1,2}$ according to equations in chapter. 2.

4.4 Blade Element Momentum Method

The next step in the design process is to choose an airfoil profile for the individual blade segments. Currently, *C-Fan*, is equipped to handle only four digit NACA airfoil profiles. For this work NACA 3510 airfoil profile is used for all blade-segments along the rotor blade span.

The airfoil polar curves are computed with the public domain code XFOIL by Drela [60]. XFOIL requires as input the airfoil name, Re, Ma, and N_{crit} to output the airfoil polar curves for a range of angle of attack. N_{crit}, is the critical amplification factor and is a parameter used in XFOIL to control the transition between laminar and turbulent flow over the airfoil surface. A higher N_{crit} value represents a less

sensitive flow, i.e., more likely to remain laminar, while a lower N_{crit} value represents a more sensitive flow, i.e., more likely to transition to turbulent. The choice of N_{crit} value can significantly impact the computed drag and lift coefficients, as turbulent flow has higher skin friction drag compared to laminar flow. In XFOIL, the default N_{crit} value is 9. However, it can be adjusted by the user to better match experimental data or simulate different flow conditions. Choosing the appropriate N_{crit} value can be challenging, as it depends on factors such as airfoil geometry, flow conditions, and surface roughness. For this work, N_{crit} is set to a value of 6, which corresponds to experiments conducted in a dirty wind-tunnel.

An initial guess is made for Re, and the corresponding airfoil polar curves are obtained for a range of angle of attack from 0° (α_i) to 15° (α_f), in steps of 0.1° (α_{step}). The angle of attack is chosen such that minimum drag-to-lift ratio ($\varepsilon = C_D/C_L$) is achieved at every blade-segment. All inputs required by XFOIL to output the airfoil polar curves is tabulated in Tab. 4.5.

Table 4.5: XFoil Inputs

Parameter	Value
Airfoil	NACA3510
Re	1.5E+05
Ma_{tip}	0.165
N_{crit}	6
α_i	0°
α_f	15°
α_{step}	0.1°

All inputs required for the computation of the blade solidity (σ) using the BEM method, according to Eq. (2.41) is now available. The blade solidity, blade spacing (s_b), and blade chord length (l_c) can be calculated at all blade spans. Once the chord length (l_c), is calculated for all blade segments, the Reynolds number at all blade spans is calculated according to Eq. (4.5).

$$Re_l = \frac{w_\infty l_c}{\nu} \tag{4.5}$$

The Reynolds number obtained according to Eq. (4.5), is then compared to the initially assumed Reynolds number which were used to obtain the polar curves from XFOIL. The initial Reynolds number is iteratively updated, and the corresponding polar curves are obtained till the initial Reynolds number and that obtained using Eq. (4.5) are within 0.1 % of one another. Ultimately, the Reynolds number calculated for each blade segment using the chord length (l_c), according to Eq. (4.5), must agree with Reynolds number used to obtain the polar curves for the chosen airfoil.

Once the blade chord length is determined the twist of the blade along the blade span is calculated, i.e., the stagger angle (γ in Fig. 2.8) for each individual blade segment. The stagger angle of each blade segment is calculated as the sum of the angle of attack (α) and the vectorial mean flow angle (β_∞), according to Eq. (2.46).

4.5 Design Check

The initial choice of blade count (z_b) and hub diameter (d_{hub}) is now verified. Flow separation is a common concern in fan and compressor design, as the flow experiences an unfavorable pressure gradient as it moves through the blade passage. To check the validity of the design, a few design criteria must be fulfilled by the final design.

The DeHaller criterion [83] is a commonly employed design criteria check, to limit the flow diffusion within the blade passage. The DeHaller number is defined as the ratio of the relative velocity at rotor exit to rotor inlet, according to Eq. (4.6). It is recommended to keep the DeHaller number greater than 0.72, at all blade spans. However, this is especially true at the hub, where the maximum flow diffusion is expected. Marcinowski [84] and Schiller [85], suggest limiting the flow diffusion at the rotor hub to between $0.55 - 0.60$, for single-stage fans to prevent flow separation at the hub. If the design criteria, is not met at the end of the design process, the initial basic design parameters must be reconsidered.

Additionally, an attempt must be made to ensure that the chord based Reynolds number, is maintained above $1.5E+05$. And the blade solidity should be maintained below 0.7 at all blade sections. For small diameter, and slow rotating fans both the Reynolds number and solidity requirements at the hub is difficult to achieve.

The four different designs have been compared in Fig. 4.2 and Fig. 4.3. Complete design data is provided in the Sec. 6.2.

$$De\ Haller = \frac{w_2}{w_1} \geq 0.72 \tag{4.6}$$

A flowchart is presented in Fig. 4.4 to outline the framework for the in-house python library, *C-Fan*. In Fig. 4.4, *Check A* refers to a comparison between the *Re* number obtained from the BEM method, and the *Re* number used to obtain the polar curves. *Check B*, refers to the DeHaller number, blade solidity and *Re* number check outlined in Sec. 2.8.

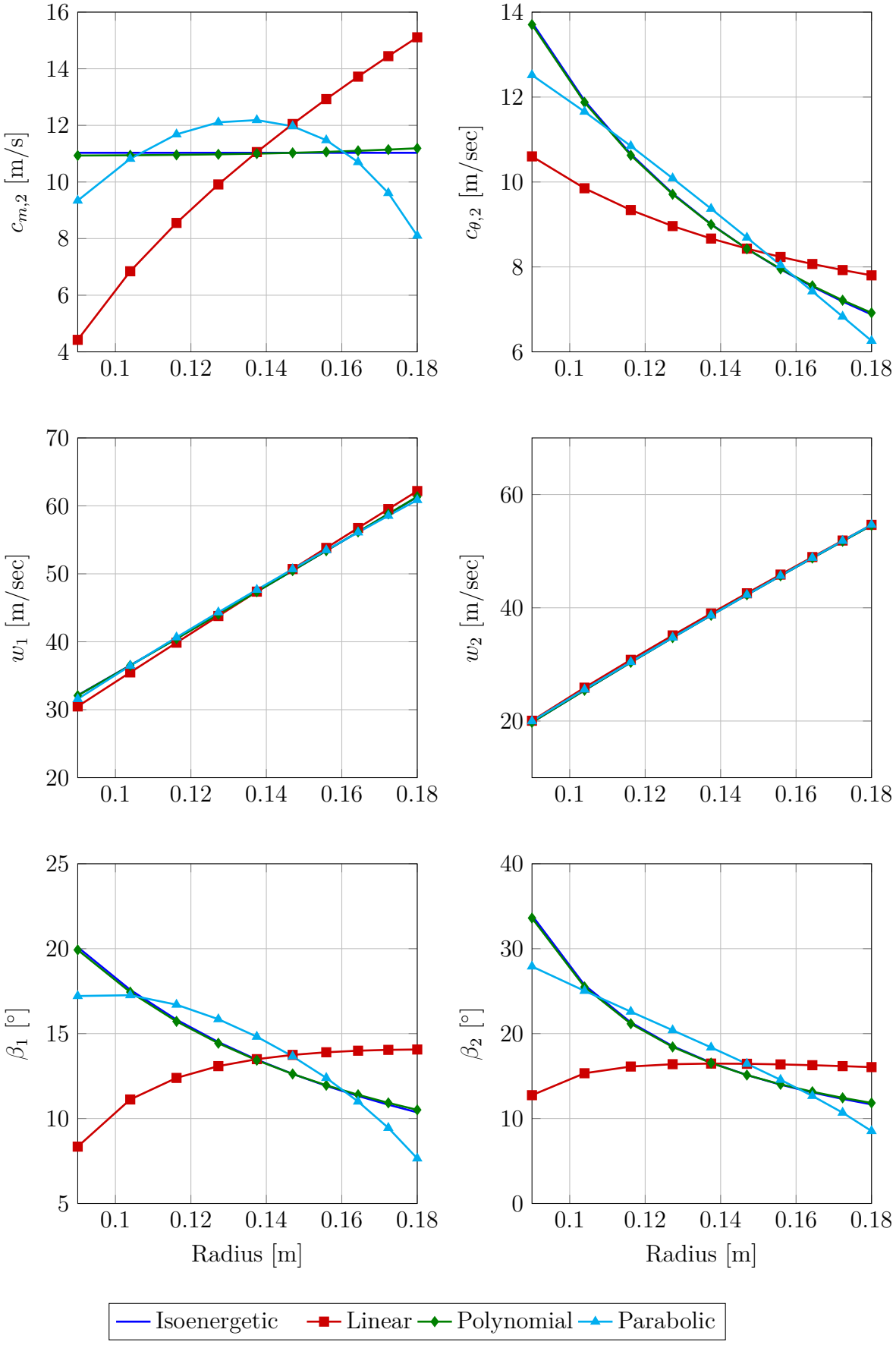

Figure 4.2: Design comparison

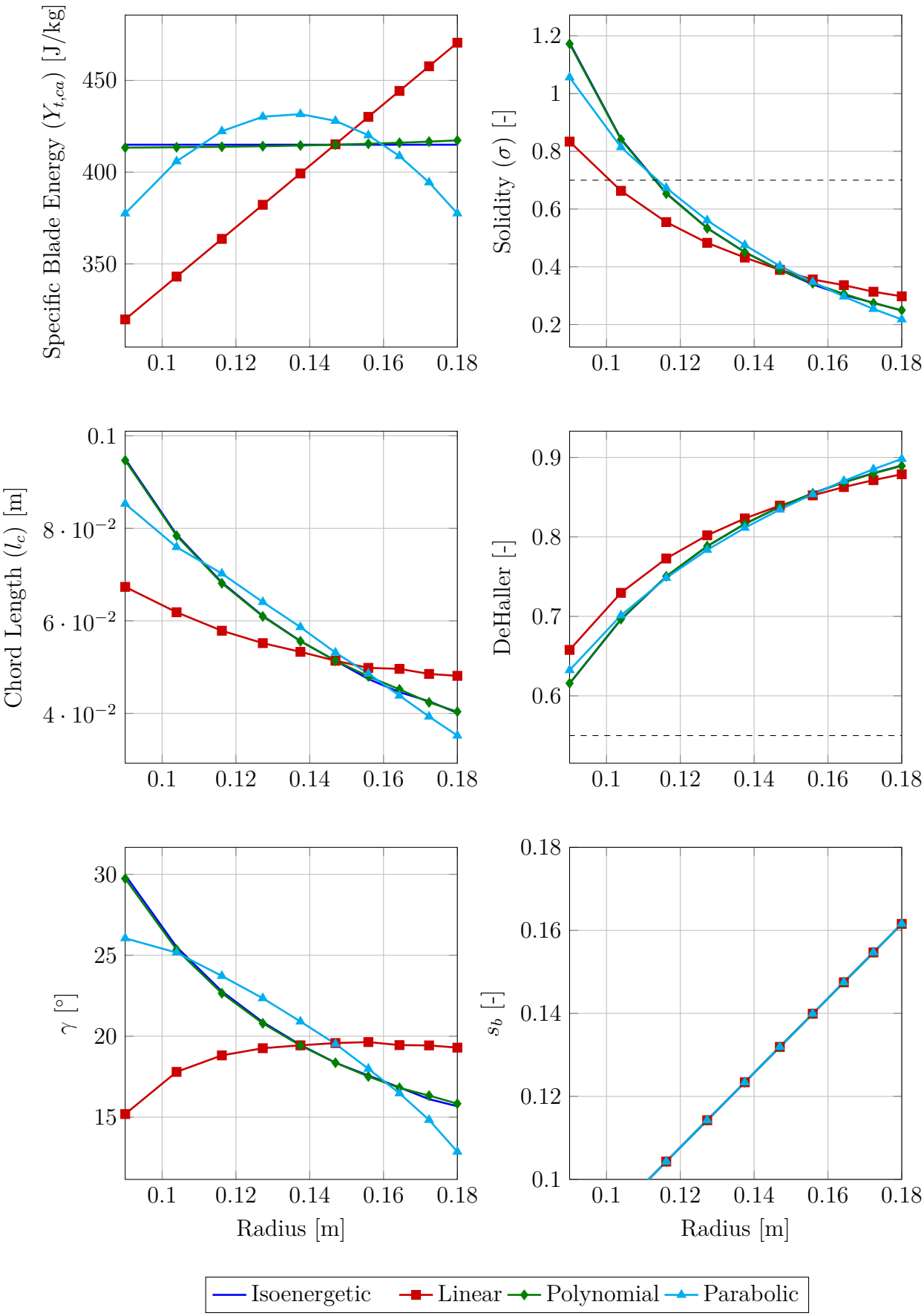

Figure 4.3: Design comparison

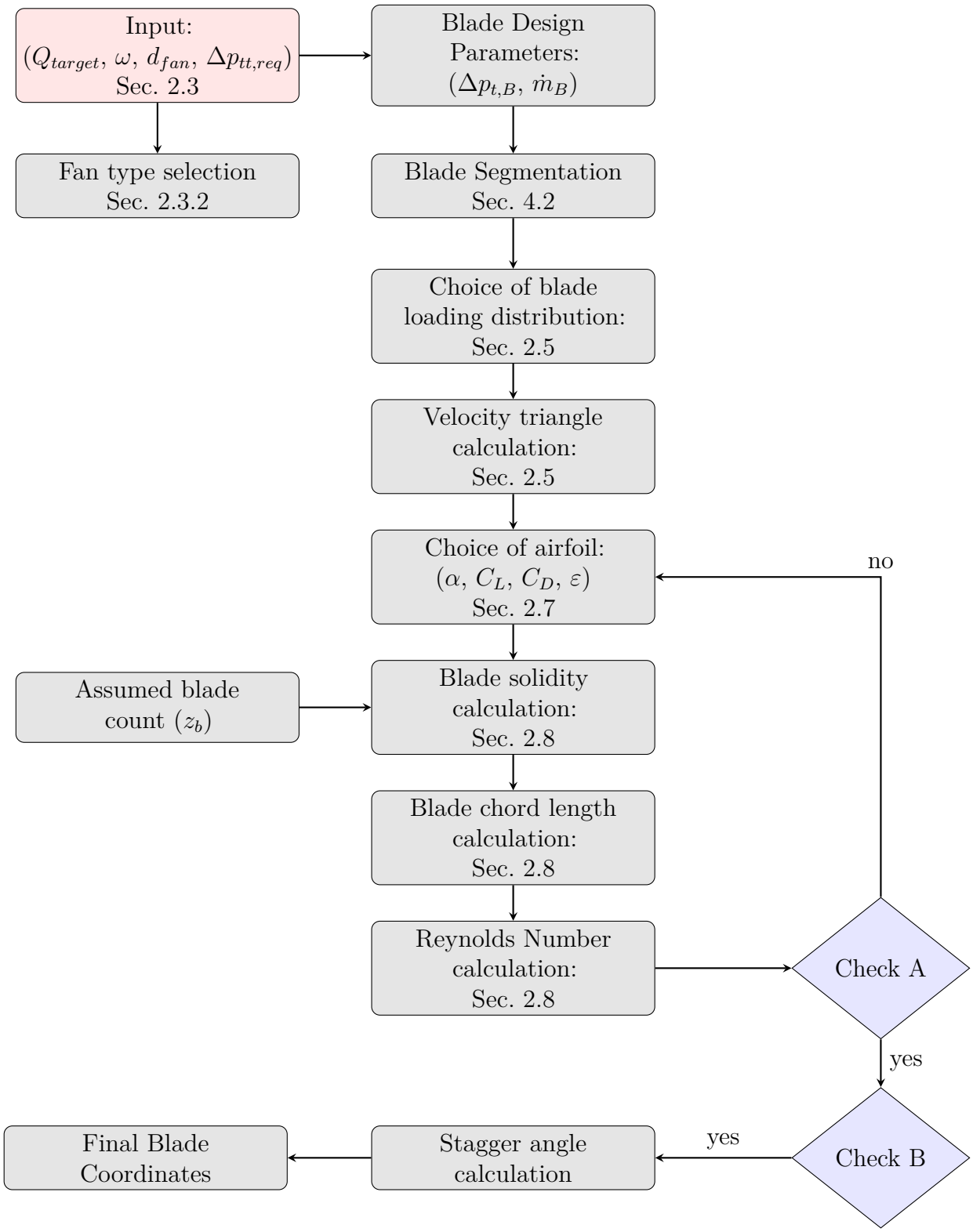

Figure 4.4: *C-Fan* framework

Chapter 5

Summary of papers

5.1 Paper 1

In Paper 1, the aerodynamic performance of a low-pressure axial fan with dimensional resemblance to an automotive cooling fan, was investigated when subjected to an upstream blockage.

5.1.1 Methodology

A ducted rotor-only low-pressure axial fan designed and experimentally tested at Friedrich-Alexander University (FAU) was used for this work [42, 43]. The experimental characteristic curve for a single rotational speed and the three velocity components, i.e., axial, radial and circumferential velocity components at the rotor inlet and outlet was made publicly available by FAU.

The first part of this work focused on the numerical validation of the experimental data from FAU. Three-dimensional, steady state Reynolds-Averaged Navier Stokes (RANS) analysis was performed on a single blade passage for the validation study. The inlet nozzle, the downstream diffusor and the fan-hub cap were included in the Computational Fluid Dynamics (CFD) domain. The structural struts, the hub fillet, and the downstream motor was excluded from the CFD domain, instead the hub was extended to the CFD domain outlet. The choice of turbulence model was investigated. The three commonly used RANS turbulence models, i.e., $k-\varepsilon$, $k-\omega$, and the SST turbulence model were used to simulate the characteristic curve for all experimental operating points till the onset of stall.

Once good agreement was achieved between the numerical and experimental data, the effect of a generic upstream blockage was investigated. A generic blockage in the form of a circular disc was placed upstream to the fan. Three different radial extents of the circular disc was considered, such that the disc blocked 25%, 50% and 75% of the rotor blade span. The axial position of the circular disc upstream to the fan, was maintained at a constant value for all three cases.

5.1.2 Discussion

The validation study yields a good comparison between the numerical data and the experimental data from FAU. Of the three investigated turbulence models, $k-\varepsilon$, was chosen to be the turbulence model of choice. This choice is attributed to the $k-\omega$ and the SST turbulence model exhibiting bi-directional error when compared to the experimental data at overload conditions. Additionally, the $k-\omega$ and the SST turbulence model, predicted an early and sharp onset of stall compared to the experimental data. In comparison, the $k-\varepsilon$ turbulence model, under-predicted both the total-to-static pressure coefficient and the total-to-static efficiency for all experimental data points.

A good agreement was achieved between the meridional velocity component at both the rotor inlet and outlet, except at the tip region where RANS models are predictably limited due to the presence of tip vortices. However, a difference was observed in the circumferential velocity component at the rotor inlet. CFD predicted a swirl-free inlet. In comparison, a negative circumferential velocity component, increasing from the blade mid-span to the tip was observed in the experiments. Here it is concluded, that the circumferential velocity component observed in the experiments performed at FAU, was an experimental artifact, possibly a result of the model or rig construction and therefore not predicted by CFD.

The validated numerical setup was used to study the effect of upstream blockage on aerodynamic performance of low-pressure axial fans. The presence of an upstream blockage, predictably led to the formation of a re-circulation region at the rotor hub and flow re-distribution along the blade span. Increasing the radius of the circular disc, led to a decrease in the meridional velocity component at the hub and corresponding, which consequently led to an increase in the meridional velocity at higher blade spans. The aerodynamic performance of the rotor, i.e., the total-to-static pressure and the total-to-static efficiency decreased significantly with increase in the radius of the circular disc. Additionally, the peak total-to-static efficiency was observed to move to a lower flow coefficient, with an increase in the in the radius of the circular disc.

5.1.3 Division of work

All numerical investigations were performed by Debarshee Ghosh. Professor Niklas Andersson provided technical supervision for all parts of the work. Associate Professor Sassan Etemad provided project supervision. The geometry and experimental results used in this work were obtained from FAU [42, 43].

5.2 Paper 2

As discussed in Ch. 1, it is a common practice to place multiple cooling fans in parallel as a part of the cooling package, in close proximity to one another. The tightly packed underhood region and heat-exchanger shape limit the fan diameter. In order to circumvent this limitation, multiple cooling fans of small diameters are tightly

packaged and placed in parallel. Paper 2 numerically investigates the aerodynamic performance of two low-pressure axial fans installed in parallel in comparison to a single-fan.

5.2.1 Methodology

The geometry from FAU used in Paper 1 is also used in this work. Two low-pressure axial fans are placed parallel to one another, with their rotational axes separated by 1.35 times the casing diameter. This is the closest the two fans can be positioned without the inlet nozzles coming into contact. The two fans are placed in identical axial positions, are considered to rotate in the same direction, and operate at the same aerodynamic operating point.

First, a validation study is performed against the experimental results from FAU for a single-fan. Specifically, the numerically obtained aerodynamic performance parameters and the radial distribution of the velocity components at the rotor inlet are compared with experimental data from FAU. Full-annulus, three-dimensional, Unsteady RANS (URANS) analysis with the $k-\varepsilon$ turbulence model is conducted to obtain the numerical results. The motion of the fan is modeled using the sliding grid approach.

The validated numerical setup for a single-fan is then used to investigate the aerodynamic performance of two fans installed in parallel. For both the single-fan and two-fans-in-parallel cases, only the experimental BEP is investigated numerically, due to the significantly large grid size and small time-step required for the simulations. An auto-correlation study is performed on the pressure signals obtained from the two fans to identify any coupling of their pressure fields.

5.2.2 Discussion

The validation study performed for a single-fan provides a good comparison with the experimental data from FAU. Minimal differences are observed in the aerodynamic performance parameters compared to experimental data at BEP. An almost identical match is obtained for the meridional velocity component both upstream and downstream of the rotor. A difference is observed in the circumferential component of velocity at the rotor inlet. Similar to the results from Paper 1, CFD predicts zero circumferential velocity along the blade span at the rotor inlet, whereas experimental data shows an increasing negative circumferential velocity component from the blade mid-span to the tip.

The validated numerical setup is then used to investigate the aerodynamic performance of two fans in parallel. A local diffusion of the flow is observed at the inlet nozzle, in the region where the two fans are closest to one another. The local diffusion zone forms as a result of the two fans competing for the mass flow of air. This local diffusion zone leads to a circumferential non-uniformity of the flow at the nozzle inlet. The circumferential non-uniformity is not identical across the two fans and also exhibits temporal variation. Although the temporal variation is minimal, a phase difference is observed between the two fans.

The pressure fields of the two fans exhibit strong coupling, with the maximum correlation observed for a time lag corresponding to the time taken for the rotor blade to travel half the blade passage. The non-uniformity is quantified at the nozzle inlet in space and time using distortion indices: Radial Distortion Index (RDI) and Circumferential Distortion Index (CDI).

The acceleration of the flow through the nozzle allows it to re-establish spatial homogeneity before reaching the rotor leading edge (LE). Ultimately, no significant differences are observed in the circumferentially and time-averaged velocity components at the rotor inlet. As a result, only minor differences are noted in the aerodynamic performance of the two fans installed in parallel, both relative to each other and compared to a single-fan operating in stand-alone mode. It is concluded that two geometrically identical fans, operating at identical aerodynamic points and rotating in the same direction, behave nearly identically to a single-fan in stand-alone operation.

5.2.3 Division of work

All numerical investigations were performed by Debarshee Ghosh. Professor Niklas Andersson provided technical supervision for all parts of the work. Associate Professor Sassan Etemad provided project supervision. The geometry and experimental results used in this work were obtained from FAU [42, 43].

5.3 Paper 3

Paper 3 extends the work performed on low-pressure axial fans installed in parallel and evaluates the changes in acoustic characteristics resulting from placing two-fans in parallel compared to a single-fan operating in stand-alone mode.

5.3.1 Methodology

The geometry from FAU [42, 43] used in Paper 1 and Paper 2 is also used in this work. Two low-pressure axial fans are placed parallel to one another, with the rotational axes separated by 1.35 times the casing diameter. Axially, the fans are positioned at the same location, rotate in the same direction, and operate at the same aerodynamic operating point.

First, a numerical validation study is done for a single-fan. The numerical results are compared against the aerodynamic and aeroacoustic experimental results from FAU. The experimental data from FAU includes aerodynamic performance parameters, detailed flow measurements using a two-component Laser Doppler Anemometry (LDA) system, wall pressure fluctuation data from 15 wall pressure transducers mounted flush with the stationary casing, and far-field sound measurements from seven microphones arranged in a half-circle with a radius of 1 m upstream of the bell-mouth inlet.

Full-annulus, three-dimensional, transient, scale-resolving simulations are conducted using Delayed Detached Eddy Simulations (DDES) as the turbulence model.

The far-field sound is computed using hybrid computational aeroacoustic methods. Specifically, the permeable FWH method with the Farassat-1A analogy is used to predict the far-field sound. The fan motion is modeled using the sliding grid approach.

The validated numerical setup for a single-fan is then used to investigate the aeroacoustic performance of two-fans installed in parallel. For both the single-fan and two-fans in parallel cases, numerical investigations are performed only at the experimental BEP.

5.3.2 Discussion

The validation study for a single-fan yields good agreement with both the aerodynamic and acoustic experimental data from FAU. Minimal differences are observed in the aerodynamic performance parameters and velocity components at the rotor inlet compared to the experimental data at BEP. Strong agreement is achieved for the wall pressure fluctuations recorded by the transducers mounted flush with the stationary casing. In the computational domain, the wall pressure probes are positioned in the Direct Noise Calculation (DNC) region, i.e., enclosed by the permeable FWH surface. All tonal components associated with the BPF and its harmonics are accurately captured in the DNC region of the domain.

The far-field noise, obtained using the hybrid acoustic analogy, predicts the far-field sound reasonably well. The dominant noise source of the fan, subharmonic tip noise, is captured accurately. However, the numerical setup shows limitations in predicting the low-frequency part of the acoustic spectrum ($f < 300$ Hz) compared to experimental data. Specifically, the numerical results over-predict the low-frequency noise.

The validated numerical setup is used to investigate the aeroacoustic performance of two-fans placed in parallel. A local flow diffusion is observed at the inlet nozzle in the region where the two-fans are closest to each other, similar to the observations made in Paper 2. However, due to the higher spatial and temporal resolution required for aeroacoustic simulations, a previously unidentified vortex is found bounding the local diffusion zone. This vortex is observed to shed directly into the tip region of the two-fans. Similar to the findings from Paper 2, the aerodynamic performance of the two-fans in parallel remains almost identical to that of a single-fan.

For the two-fans-in-parallel case, a significant increase in the overall sound power level (SWL) of 6.3 dB is observed compared to a single-fan. The acoustic spectra for two-fans in parallel, scales in accordance with having two equally strong, independent sound sources. No significant changes are observed in the acoustic characteristics for two-fans in parallel compared to a single-fan for frequencies greater than 300 Hz. However, some minor differences are observed in the low-frequency region ($f < 300$ Hz) of the acoustic spectra when two-fans are placed in parallel, as a result of the presence of a local diffusion zone in the region where the two-fans are closest to one another.

Ultimately, this work concludes that for rotor-only LPA fans with a stationary shroud and inlet bell-mouth, operating in the low subsonic flow regime, an amplifica-

tion in the overall SWL of 6 dB is expected as a result of placing them in parallel, with marginal changes to the low-frequency region of the acoustic spectrum compared to a single-fan operating in stand-alone mode.

5.3.3 Division of work

All numerical investigations were performed by Debarshee Ghosh. Michail Vourakis provided technical guidance for interpreting the experimental results from FAU. Professor Niklas Andersson provided technical supervision for all parts of the work. Associate Professor Sassan Etemad provided project supervision. The geometry and experimental results used in this work were obtained from FAU [42, 43].

5.4 Paper 4

As discussed in Ch. 1, low-pressure axial fans are often placed in tightly packed underhood regions. Their placement often limits the inclusion of large inlet nozzles, which condition the flow ingested by the rotor, especially in the rotor tip region. Bell-mouths ensure spatial homogeneity of the flow entering the rotor by eliminating large-scale flow structures that negatively affect both the aerodynamic and acoustic performance of the fan. This work computationally investigates the effect of the inlet-nozzle radius on both sub-harmonic and broadband tip noise.

5.4.1 Methodology

The geometry from FAU used in Papers 1-3 is used again for this work. Modifications are made to the inlet nozzle of the baseline design. Geometrically, the inlet nozzle is a quarter circle. Within the scope of this work, the ratio of the inlet-nozzle-diameter to the duct-diameter is referred to as the nozzle-diameter ratio ($d_{nz,ratio}$). The baseline geometry has a nozzle-diameter ratio of 0.2. Three different nozzle-diameter ratios are investigated, i.e., 0.1, 0.2, and 0.3. An additional case with no inlet nozzle ($d_{nz,ratio} = 0.0$), resulting in a sharp intake, is also investigated.

Full-annulus, three-dimensional, scale-resolving, transient simulations are conducted using DDES as the turbulence model. The far-field sound is computed using hybrid computational aeroacoustic methods. Specifically, the permeable FWH method with the Farassat-1A analogy is used to predict the far-field sound. The fan motion is modeled using the sliding grid approach.

The change in aeroacoustic performance as a result of varying the diameter of the inlet nozzle is quantified through changes in aerodynamic performance parameters, radial distribution of velocity components at the rotor inlet, overall SWL, and acoustic characteristics.

5.4.2 Discussion

The aerodynamic performance of the rotor, influenced by changes in the inlet bell-mouth radius, was quantified using the total-to-total pressure rise (p_{tt}) and

total-to-total efficiency (η_{tt}). Both performance parameters decrease proportionally with a reduction nozzle-diameter-ratio. The total-to-total pressure rise decreases by 18%, and the total-to-total efficiency reduces by 7% when comparing the largest and smallest investigated inlet bell-mouth radii.

For the smallest investigated nozzle diameters, i.e., $d_{nz,ratio} = 0.1$ and 0.0, significant flow separation is observed in the tip region. This flow separation causes a substantial redistribution of the flow to lower blade spans, an increase in circumferential velocity, and higher vorticity in the tip region. The vorticity in the tip region is quantified using Q-criterion. The decrease in meridional velocity and the increase in circumferential velocity result in a higher swirl angle at the rotor tip. The increased swirl angle leads to a larger angle of incidence at the rotor tip region, promoting the formation of stronger tip vortices. The overall sound power level (SWL) increases by 3.4 dB between the smallest and largest investigated nozzle-diameter-ratio.

A decrease in the inlet nozzle radius results in an increase in low-frequency noise ($f < 1$ kHz) due to greater turbulence ingestion caused by flow separation at the inlet nozzle. However, decreasing the nozzle-diameter-ratio also reduces the dominance of sub-harmonic tip noise. This reduction occurs as a result of the increased turbulent structures at the tip region, caused by flow separation, which in turn suppresses the formation of coherent tip structures responsible for subharmonic tip noise. Additionally, a decrease in the inlet nozzle radius reduces noise within the frequency range of $1 - 2$ kHz, which is dominated by tip noise. Here it is also noted that, no significant differences are observed in the acoustic characteristics for the two largest investigated nozzle-diameter-ratios, i.e., $d_{nz,ratio} = 0.2$ and 0.3.

5.4.3 Division of work

All numerical investigations were performed by Debarshee Ghosh. Professor Niklas Andersson provided technical supervision for all parts of the work. Associate Professor Sassan Etemad provided project supervision. The baseline geometry used in this work were obtained from FAU [42, 43].

5.5 Paper 5

Cooling-fans in electric vehicles are installed in increasingly compact underhood spaces, where manufacturers seek greater flexibility to position the fan in areas that may partially or fully obstruct the fan inlet. Typically, the air entering the underhood region passes through the grill, charger cooler, and heat-exchanger before being ingested by the fan, often resulting in a spatially non-homogeneous and turbulent flow at the fan inlet. This work aims to evaluate the ability of the hybrid computational aeroacoustic methods to capture changes in the aeroacoustic characteristics of an automotive cooling fan when subjected to upstream blockages by comparing against experimental data.

5.5.1 Methodology

An in-service automotive cooling fan with a rotating ring and downstream stators is used for the numerical investigations in this work. Full-annulus, three-dimensional, transient, scale-resolving simulations are performed using DDES as the turbulence model. The far-field sound is computed using hybrid computational aeroacoustic methods, specifically the permeable FWH method with the Farassat-1A analogy. The fan motion is modeled using the sliding grid approach.

First, a validation study is conducted, where the numerically obtained aerodynamic and aeroacoustic data are compared to experimental data for three aerodynamic operating points: aerodynamic BEP, free-discharge operating point, and an operating point between the BEP and free-discharge point. The validated numerical setup is then used to investigate the effect of upstream blockage. A generic upstream blockage in the form of a solid 60° solid is placed just upstream of the fan.

5.5.2 Discussion

The validation study concluded that the numerical setup used in this work successfully predicts the aerodynamic performance of the in-service cooling fan at aerodynamic operating points away from the free-discharge conditions for clean inlet flow conditions. The used numerical setup, however, fails to accurately capture the free-discharge operating point compared to experiments, and under-predicts the effect of the blockage.

Both numerical and experimental data capture the upward scaling of the acoustic spectra as a result of decreasing the inlet volume flowrate. For all three operating points, the numerical setup accurately captures the base broadband noise levels. For all three operating points, the high frequency broadband noise region ($f > 5\ kHz$), which is typically dominated by boundary layer noise and TE noise, is marginally under-predicted by CFD. The mid-frequency broadband noise spectra between 1-5 kHz compares well with experimental data for all three operating points. The low-frequency base broadband level is marginally over-predicted by CFD for all three investigated operating points. The numerical data accurately captures the BPF for all operating points. Both experimental and numerical data, accurately capture the reduced dominance of the narrow band hump associated with subharmonic tip noise at higher flowrates.

The numerical data accurately captures the base broadband noise levels for the upstream blockage case. However, it is unable to accurately capture the increase in the tonal peaks at shaft rotational frequency observed in the experimental data. This under-prediction in the tonal peaks by the numerical data is assumed to be a result of the numerical setup under-predicting the effect of the blockage, flow separation, and therefore spatial non-homogeneity, and turbulence levels.

5.5.3 Division of work

Numerical investigations were performed by Debarshee Ghosh, Ashik Roy, and Alexander Boström. All experimental investigations were performed by Michail

Vourakis. Professor Niklas Andersson provided technical supervision for all parts of the work. Associate Professor Sassan Etemad provided project supervision. The geometry and experimental results used in this work were obtained from FAU [42, 43].

5.6 Paper 6

Several scientific studies have illustrated, through both numerical and experimental investigations, the detrimental effect on the aerodynamic and aeroacoustic performance of low-pressure axial fans ingesting spatially non-uniform flow [25–30] and/or turbulent inflow [31–37]. Conversely, limited scientific works focus on the aerodynamic performance of a LPA fan with radius-dependent blade-loading distribution subjected to a non-uniform inlet profile. Additionally, limited numerical work focus on the isolated effect of radius-dependent blade loading distribution on the aeroacoustic performance of the fan.

5.6.1 Methodology

In this study, four distinct rotor blade geometries with varying blade-loading distributions are generated using the Blade Element Momentum (BEM) method for low-solidity fans [38, 43, 44]. The blade designs are created using an in-house Python code, *C-Fan*, ensuring they are both geometrically and operationally representative of fans utilized in automotive thermal management systems.

The first part of this study focuses on the computational evaluation of the different rotor blade designs under both spatially uniform and non-uniform inlet flow conditions. For the non-uniform inlet flow, a generic velocity profile similar to that reported in Paper-1 is imposed at the computational domain's inlet. The profile documented in Paper-1 is characteristic of flow conditions when a fan operates in the presence of an axi-symmetric upstream blockage, blocking a portion of the blade span. Two distinct non-uniform inlet profiles are examined. Aerodynamic performance is analyzed through a three-dimensional, steady-state Reynolds-Averaged Navier-Stokes (RANS) simulation of a single blade passage, employing the Spalart-Allmaras turbulence model. Two non-uniform inlet profiles are considered: one with maximum inlet meridional velocity near the tip and another with maximum inlet velocity at mid-span.

The second part of this study involves three-dimensional, full annulus, transient, scale-resolving simulations using the Delayed Detached Eddy Simulation (DDES) turbulence model to predict the acoustic signature of the four rotor designs under spatially uniform inlet flow conditions. The far-field noise is computed using the permeable Ffowcs-Williams Hawkings (FWH) analogy, specifically utilizing the Farassat-1A formulation. The variation in the acoustic signature of the fan is assessed by quantifying changes in the overall sound power level (SWL, L_w) and changes in the far-field acoustic spectra. Investigations are only performed for the ADP.

5.6.2 Discussion

For the aerodynamic analysis of the four rotor blade designs, the isoenergetic design consistently achieves the highest efficiency (η_{ts}) and total-to-static pressure (p_{ts}), whereas the linear blade-loading design exhibits the lowest values due to flow redistribution towards the tip region, leading to minimal flow ingestion at lower blade spans.

Aeroacoustic analysis using full-annulus, transient Delayed Detached Eddy Simulations (DDES) illustrates that the linear and polynomial designs have similar acoustic characteristics. All designs exhibit dominant tones at 900 Hz and 1200 Hz, suspected to be associated with sub-harmonic tip noise. The parabolic design produces the highest low-frequency noise, while mid-frequency noise is strongest in the isoenergetic, polynomial, and parabolic designs due to higher tip-region velocity. Minimal differences are observed in high-frequency noise region of the acoustic spectra.

Despite its poor aerodynamic performance, the linear blade-loading design demonstrates the best acoustic characteristics, making it a favorable choice for noise-sensitive applications.

5.6.3 Division of work

Numerical investigations were performed by Debarshee Ghosh. Professor Niklas Andersson provided technical supervision for all parts of the work. Associate Professor Sassan Etemad provided project supervision.

Chapter 6

Conclusion

6.1 Concluding remarks

This thesis work investigates the aerodynamic and aeroacoustic performance of low-pressure axial fans that are dimensionally and operationally representative of those used in automotive cooling systems. The key focus of this work is to examine the impact of installation effects on the aerodynamic and aeroacoustic performance of these fans. In particular, the effects of upstream blockages, parallel fan configurations, and changes in inlet nozzle geometry are investigated. In addition, the design process for low-pressure axial fans is detailed using the Blade Element Momentum (BEM) method. Four rotor designs with different blade loading distributions are generated.

The investigation into upstream blockages illustrates that even moderate blockages along the rotor blade span can significantly change the flow ingested by the fan. The upstream blockages change the flow distribution along the blade span and result in the formation of recirculation zones at the rotor LE downstream of the blockage. This redistribution of flow along the rotor blade span leads to a reduction in aerodynamic efficiency and pressure rise achieved by the fan. Additionally, it is observed that the peak efficiency moves to a lower flow coefficient. Spatial non-uniformity and the formation of recirculation zones at the rotor LE can cause unsteady blade forces, which in turn can increase the sound emission of the fan.

This research work also highlights the effects of using multiple fans in parallel. In modern automotive applications, space constraints often necessitate the use of several small-diameter fans instead of a single large fan. Numerical simulations indicate that when two-fans are arranged in parallel and operate at the same aerodynamic point, their overall aerodynamic performance remains comparable to that of a single fan. It is also found that placing two-fans in parallel leads to minimal changes in the acoustic characteristics compared to a single fan. However, the overall Sound Power Level (SWL) is observed to increase significantly by 6 dB, indicating that the two-fans in parallel act as strong independent sound sources, with minimal interaction effects. These results suggest that while parallel fan configurations match the aerodynamic performance of a single fan, measures must be taken to manage the increased noise levels resulting from placing the fans in parallel.

The impact of inlet nozzle geometry on fan performance is also addressed. By varying the nozzle-diameter ratio, it is observed that smaller inlet bellmouth radii tend to promote flow separation, especially near the rotor tip region. This separation at the tip region, locally reduces the meridional velocity and increases the swirl angle. Consequently, both the pressure rise and the efficiency of the fan drop. From an acoustic standpoint, a smaller inlet nozzle is observed to raise broadband noise levels while reducing the dominance of sub-harmonic tip noise. These findings suggest that, whenever possible, the inlet nozzle should be incorporated to enhance both aerodynamic and acoustic performance.

Additionally, an in-service automotive cooling fan that includes a rotating ring and downstream stators is numerically investigated. The fan is analyzed when subjected to an upstream blockage. The numerical models capture general trends observed in experiments. The fan's aerodynamic performance is well predicted over several operating points. Some discrepancies are noted, particularly near free discharge operating conditions. The numerical approach tends to under-predict the effect of blockage on both the flow field and the tonal noise peaks. These differences highlight the challenges of accurately modeling complex flow interactions, even with high-fidelity computational methods. They also point to areas where simulation techniques can be improved in the future.

Lastly, four rotor designs with different blade-loading distribution are investigated aerodynamically for uniform and non-uniform inlet flow conditions. The aerodynamic performance of the linear blade-loading design was observed to be consistently worse compared to the other blade-loading distributions irrespective of the inlet flow profile. On the contrary, the linear blade-loading distribution yields the best acoustic performance. These results strongly indicate the influence of the rotor blade-loading distribution on both the aerodynamic and acoustic performance of low-pressure axial fans.

Ultimately, this work details the rotor design process, computational methods and their limitations for the aerodynamic and aeroacoustic analysis of low-pressure axial fans when subjected to different installation effects. This thesis work, also provides rotor blade designs, and a rotor blade design tool, i.e., *C-Fan* for future scientific work.

6.2 Future work

A key limitation of this work is the use of generic upstream blockages. Future studies with realistic upstream blockages representative of actual underhood components are recommended. For two-fans in parallel, only cases where both fans operate at identical aerodynamic operating points are investigated in this work. Future studies on configurations where fans operate at different aerodynamic operating points are highly recommended. Preliminary investigations (not presented here) on the operation of two fans in parallel, each running at a different aerodynamic operating point, suggest that the fan with the higher rotational speed dominates, drawing in significantly more air than the lower-speed fan. As a result, the fan operating at the lower rotational speed is pushed into stall conditions.

The numerical setup used in this work is found to be limited in accurately capturing the acoustic effects of upstream blockages. Further investigations into numerical methods that improve the prediction of these effects are recommended. Additionally, the effect of rotor blade-loading distribution on aeroacoustic performance requires further study. This work investigates only one set of blade-loading constants (a, m, and d). An optimization study exploring a broader range of blade-loading constants may help generalize the acoustic effects of blade-loading distribution. Additional studies into the effect of blade skew, and LE serrations which are known methods for noise reduction is also a recommended avenue for future work. Here it is noted that, *C-Fan*, already has built-in functionalities to add blade sweep and dihedral angle to rotor blade designs, i.e., forward and backward skew maybe added to the rotor design.

Appendix

Table 6.1: Blade Loading Distribution: Iso-energetic

Parameter Value	0	1	2	3	4	5	6	7	8	9
Radius [m]	0.09	0.104	0.116	0.127	0.137	0.147	0.156	0.164	0.172	0.18
Angle of attack [°]	4.6	4.6	4.6	4.6	4.6	4.6	4.7	4.7	4.6	4.7
$Y_{t,ca}$ [J/kg]	414.957	414.957	414.957	414.957	414.957	414.957	414.957	414.957	414.957	414.957
U [m/s]	30.159	34.825	38.935	42.652	46.069	49.25	52.237	55.063	57.751	60.319
$c_{m,1}$ [m/s]	11.031	11.031	11.031	11.031	11.031	11.031	11.031	11.031	11.031	11.031
c_2 [m/s]	17.635	16.238	15.338	14.708	14.241	13.881	13.593	13.359	13.165	13
$c_{\theta,2}$ [m/s]	13.759	11.916	10.658	9.729	9.007	8.426	7.944	7.536	7.185	6.879
$c_{m,2}$ [m/s]	11.031	11.031	11.031	11.031	11.031	11.031	11.031	11.031	11.031	11.031
w_1 [m/s]	32.113	36.53	40.468	44.055	47.371	50.47	53.389	56.157	58.795	61.319
w_2 [m/s]	19.765	25.427	30.353	34.722	38.669	42.288	45.647	48.79	51.755	54.566
w_∞ [m/s]	25.761	30.903	35.371	39.364	43.004	46.368	49.51	52.468	55.27	57.939
β_1 [°]	20.09	17.576	15.818	14.5	13.465	12.625	11.924	11.328	10.814	10.364
β_2 [°]	33.925	25.711	21.31	18.524	16.575	15.12	13.984	13.067	12.306	11.663
β_∞ [°]	25.353	20.913	18.172	16.274	14.863	13.762	12.874	12.136	11.512	10.975
c_l [-]	0.882	0.882	0.882	0.882	0.882	0.882	0.891	0.891	0.882	0.891
c_d [-]	0.012	0.012	0.012	0.012	0.013	0.013	0.013	0.013	0.013	0.013
c_d/c_l [-]	0.014	0.014	0.014	0.014	0.014	0.014	0.014	0.014	0.014	0.014
σ [-]	1.176	0.843	0.655	0.535	0.451	0.389	0.339	0.302	0.276	0.248
s_b [m]	0.081	0.093	0.104	0.114	0.123	0.132	0.14	0.147	0.155	0.162
l_c [m]	0.095	0.079	0.068	0.061	0.056	0.051	0.047	0.045	0.043	0.04
Re [-]	161,558	160,454	159,508	158,683	157,926	157,262	154,998	154,414	155,492	153,366
γ [degree]	29.953	25.513	22.772	20.874	19.463	18.362	17.574	16.836	16.112	15.675
De Haller [-]	0.615	0.696	0.75	0.788	0.816	0.838	0.855	0.869	0.88	0.89

Table 6.2: Blade Loading Distribution: Linear

Parameter Value	0	1	2	3	4	5	6	7	8	9
Radius [m]	0.09	0.104	0.116	0.127	0.137	0.147	0.156	0.164	0.172	0.18
Angle of attack [°]	5.1	4.9	4.8	4.7	4.6	4.6	4.6	4.4	4.4	4.3
$Y_{t,ca}$ [J/kg]	319.754	343.083	363.635	382.216	399.303	415.208	430.145	444.273	457.711	470.551
U [m/s]	30.159	34.825	38.935	42.652	46.069	49.25	52.237	55.063	57.751	60.319
$c_{m,1}$ [m/s]	4.424	6.846	8.553	9.913	11.056	12.048	12.928	13.721	14.445	15.111
c_2 [m/s]	11.488	11.997	12.664	13.363	14.048	14.705	15.328	15.918	16.476	17.006
$c_{\theta,2}$ [m/s]	10.602	9.852	9.339	8.961	8.667	8.431	8.234	8.068	7.926	7.801
$c_{m,2}$ [m/s]	4.424	6.846	8.553	9.913	11.056	12.048	12.928	13.721	14.445	15.111
w_1 [m/s]	30.482	35.491	39.864	43.789	47.377	50.702	53.813	56.747	59.53	62.183
w_2 [m/s]	20.051	25.895	30.807	35.118	39.001	42.56	45.863	48.957	51.877	54.648
w_∞ [m/s]	25.249	30.673	35.317	39.437	43.175	46.618	49.827	52.841	55.694	58.407
β_1 [°]	8.346	11.122	12.39	13.084	13.495	13.746	13.901	13.993	14.043	14.064
β_2 [°]	12.747	15.33	16.12	16.396	16.468	16.444	16.373	16.276	16.167	16.052
β_∞ [°]	10.092	12.897	14.016	14.558	14.837	14.977	15.038	15.05	15.032	14.994
c_l [-]	0.923	0.907	0.899	0.89	0.882	0.882	0.882	0.864	0.864	0.854
c_d [-]	0.015	0.014	0.014	0.013	0.013	0.012	0.012	0.012	0.012	0.011
c_d/c_l [-]	0.016	0.016	0.015	0.015	0.014	0.014	0.014	0.014	0.014	0.013
σ [-]	0.834	0.663	0.555	0.483	0.432	0.39	0.356	0.336	0.314	0.298
s_b [m]	0.081	0.093	0.104	0.114	0.123	0.132	0.14	0.147	0.155	0.162
l_c [m]	0.067	0.062	0.058	0.055	0.053	0.051	0.05	0.05	0.049	0.048
Re [-]	112,232	125,244	134,891	143,655	151,907	158,118	163,900	173,081	178,380	185,496
γ [degree]	15.192	17.797	18.816	19.258	19.437	19.577	19.638	19.45	19.432	19.294
De Haller [-]	0.658	0.73	0.773	0.802	0.823	0.839	0.852	0.863	0.871	0.879

Table 6.3: Blade Loading Distribution: Polynomial

Parameter Value	0	1	2	3	4	5	6	7	8	9
Radius [m]	0.09	0.104	0.116	0.127	0.137	0.147	0.156	0.164	0.172	0.18
Angle of attack [°]	4.6	4.6	4.6	4.6	4.6	4.6	4.6	4.6	4.7	4.7
$Y_{t,ca}$ [J/kg]	413.361	413.566	413.83	414.152	414.533	414.973	415.471	416.028	416.644	417.318
U [m/s]	30.159	34.825	38.935	42.652	46.069	49.25	52.237	55.063	57.751	60.319
$c_{m,1}$ [m/s]	10.934	10.943	10.958	10.977	11.001	11.03	11.063	11.101	11.143	11.191
c_2 [m/s]	17.533	16.149	15.266	14.655	14.212	13.88	13.625	13.428	13.275	13.157
$c_{\theta,2}$ [m/s]	13.706	11.876	10.629	9.71	8.998	8.426	7.954	7.555	7.215	6.919
$c_{m,2}$ [m/s]	10.934	10.943	10.958	10.977	11.001	11.03	11.063	11.101	11.143	11.191
w_1 [m/s]	32.08	36.504	40.448	44.042	47.364	50.47	53.396	56.171	58.816	61.348
w_2 [m/s]	19.755	25.425	30.354	34.722	38.669	42.288	45.645	48.787	51.75	54.56
w_∞ [m/s]	25.744	30.891	35.362	39.358	43.001	46.368	49.512	52.473	55.278	57.95
β_1 [°]	19.927	17.445	15.718	14.433	13.43	12.623	11.957	11.398	10.921	10.51
β_2 [°]	33.605	25.494	21.162	18.429	16.528	15.119	14.026	13.152	12.435	11.836
β_∞ [°]	25.133	20.748	18.052	16.194	14.823	13.761	12.911	12.213	11.63	11.134
c_l [-]	0.882	0.882	0.882	0.882	0.882	0.882	0.882	0.882	0.891	0.891
c_d [-]	0.012	0.012	0.012	0.012	0.012	0.013	0.013	0.013	0.013	0.013
c_d/c_l [-]	0.014	0.014	0.014	0.014	0.014	0.014	0.014	0.014	0.014	0.014
σ [-]	1.172	0.84	0.653	0.534	0.45	0.39	0.343	0.306	0.274	0.25
s_b [m]	0.081	0.093	0.104	0.114	0.123	0.132	0.14	0.147	0.155	0.162
l_c [m]	0.095	0.078	0.068	0.061	0.056	0.051	0.048	0.045	0.042	0.04
Re [-]	160,883	159,858	159,023	158,349	157,768	157,267	156,860	156,522	154,618	154,402
γ [degree]	29.733	25.348	22.652	20.794	19.423	18.361	17.511	16.813	16.33	15.834
De Haller [-]	0.616	0.697	0.75	0.788	0.816	0.838	0.855	0.869	0.88	0.889

Table 6.4: Blade Loading Distribution: Parabolic

Parameter Value	0	1	2	3	4	5	6	7	8	9
Radius [m]	0.09	0.104	0.116	0.127	0.137	0.147	0.156	0.164	0.172	0.18
Angle of attack [°]	4.7	4.7	4.5	4.5	4.5	4.6	4.6	4.7	4.8	4.8
$Y_{t,ca}$ [J/kg]	377.509	405.905	422.31	430.198	431.631	427.955	420.103	408.755	394.424	377.509
U [m/s]	30.159	34.825	38.935	42.652	46.069	49.25	52.237	55.063	57.751	60.319
$c_{m,1}$ [m/s]	9.343	10.82	11.683	12.107	12.186	11.969	11.476	10.702	9.61	8.103
c_2 [m/s]	15.619	15.903	15.942	15.758	15.372	14.791	14.014	13.025	11.79	10.239
$c_{\theta,2}$ [m/s]	12.517	11.656	10.846	10.086	9.369	8.689	8.042	7.423	6.83	6.259
$c_{m,2}$ [m/s]	9.343	10.82	11.683	12.107	12.186	11.969	11.476	10.702	9.61	8.103
w_1 [m/s]	31.573	36.467	40.65	44.337	47.654	50.684	53.483	56.094	58.545	60.86
w_2 [m/s]	19.963	25.571	30.422	34.743	38.67	42.29	45.661	48.827	51.82	54.664
w_∞ [m/s]	25.662	30.95	35.49	39.509	43.141	46.473	49.563	52.455	55.179	57.76
β_1 [°]	17.212	17.259	16.702	15.848	14.817	13.66	12.391	10.999	9.448	7.651
β_2 [°]	27.904	25.032	22.584	20.395	18.369	16.441	14.557	12.661	10.688	8.524
β_∞ [°]	21.35	20.462	19.219	17.845	16.408	14.925	13.388	11.773	10.03	8.064
c_l [-]	0.89	0.891	0.873	0.873	0.873	0.882	0.882	0.891	0.9	0.899
c_d [-]	0.013	0.013	0.012	0.012	0.012	0.012	0.012	0.013	0.013	0.014
c_d/c_l [-]	0.015	0.014	0.014	0.014	0.014	0.014	0.014	0.014	0.015	0.015
σ [-]	1.056	0.814	0.673	0.561	0.475	0.403	0.347	0.297	0.254	0.218
s_b [m]	0.081	0.093	0.104	0.114	0.123	0.132	0.14	0.147	0.155	0.162
l_c [m]	0.085	0.076	0.07	0.064	0.059	0.053	0.049	0.044	0.039	0.035
Re [-]	144,491	155,146	164,497	167,077	166,991	162,999	158,996	151,760	143,144	134,214
γ [degree]	26.05	25.162	23.719	22.345	20.908	19.525	17.988	16.473	14.83	12.864
De Haller [-]	0.632	0.701	0.748	0.784	0.811	0.834	0.854	0.87	0.885	0.898

Bibliography

[1] European Commission, Directorate-General for Mobility and Transport. *Transport in the European Union: Greenhouse Gas Emissions Report 2024*. Accessed: January 31, 2025. 2024. URL: https://transport.ec.europa.eu/document/download/ee264fc5-ec49-4751-9d92-08c038856ce1_en?filename=MI-AA-24-001-EN-N.pdf (cit. on p. 3).

[2] *Paris Agreement*. URL: https://treaties.un.org/pages/ViewDetails.aspx?src=TREATY&mtdsg_no=XXVII-7-d&chapter=27&clang=_en (visited on 03/28/2019) (cit. on p. 3).

[3] Julio A. Sanguesa, Vicente Torres-Sanz, Piedad Garrido, Francisco J. Martinez, and Johann M. Marquez-Barja. "A Review on Electric Vehicles: Technologies and Challenges". In: *Smart Cities* 4.1 (2021), pp. 372–404. ISSN: 2624-6511. DOI: 10.3390/smartcities4010022 (cit. on p. 3).

[4] European Alternative Fuels Observatory. *Vehicles and Fleet in the European Union (EU-27)*. Accessed: January 31, 2025. 2024. URL: https://alternative-fuels-observatory.ec.europa.eu/transport-mode/road/european-union-eu27/vehicles-and-fleet (cit. on p. 3).

[5] *Global EV Outlook 2022 – Analysis*. 2022. URL: https://www.iea.org/reports/global-ev-outlook-2022 (cit. on p. 3).

[6] Xiao Shi, Jian Pan, Hewu Wang, and Hua Cai. "Battery electric vehicles: What is the minimum range required?" In: *Energy* 166 (2019), pp. 352–358. ISSN: 0360-5442. DOI: https://doi.org/10.1016/j.energy.2018.10.056 (cit. on p. 3).

[7] Jianan Zhang, Lei Zhang, Fengchun Sun, and Zhenpo Wang. "An Overview on Thermal Safety Issues of Lithium-ion Batteries for Electric Vehicle Application". In: *IEEE Access* 6 (2018), pp. 23848–23863. DOI: 10.1109/ACCESS.2018.2824838 (cit. on p. 3).

[8] Sergio Manzetti and Florin Mariasiu. "Electric vehicle battery technologies: From present state to future systems". In: *Renewable and Sustainable Energy Reviews* 51 (2015), pp. 1004–1012 (cit. on p. 4).

[9] A Perner and J Vetter. "Lithium-ion batteries for hybrid electric vehicles and battery electric vehicles". In: *Advances in battery technologies for electric vehicles*. Elsevier, 2015, pp. 173–190 (cit. on p. 4).

[10] ÁG Miranda and CW Hong. "Integrated modeling for the cyclic behavior of high power Li-ion batteries under extended operating conditions". In: *Applied energy* 111 (2013), pp. 681–689 (cit. on p. 4).

[11] Yonghuang Ye, Yixiang Shi, and Andrew AO Tay. "Electro-thermal cycle life model for lithium iron phosphate battery". In: *Journal of Power Sources* 217 (2012), pp. 509–518 (cit. on p. 4).

[12] Riza Kizilel, Rami Sabbah, J Robert Selman, and Said Al-Hallaj. "An alternative cooling system to enhance the safety of Li-ion battery packs". In: *Journal of Power Sources* 194.2 (2009), pp. 1105–1112 (cit. on p. 4).

[13] Ahmad A Pesaran. "Battery thermal models for hybrid vehicle simulations". In: *Journal of power sources* 110.2 (2002), pp. 377–382 (cit. on p. 4).

[14] Zhonghao Rao, Shuangfeng Wang, Maochun Wu, Zirong Lin, and Fuhuo Li. "Experimental investigation on thermal management of electric vehicle battery with heat pipe". In: *Energy Conversion and Management* 65 (2013), pp. 92–97 (cit. on p. 4).

[15] Thanh-Ha Tran, Souad Harmand, and Bernard Sahut. "Experimental investigation on heat pipe cooling for hybrid electric vehicle and electric vehicle lithium-ion battery". In: *Journal of power sources* 265 (2014), pp. 262–272 (cit. on p. 4).

[16] Ahmad A Pesaran. "Battery thermal management in EV and HEVs: issues and solutions". In: *Battery Man* 43.5 (2001), pp. 34–49 (cit. on p. 4).

[17] Wensheng Huang, Xuning Feng, Xuebing Han, Weifeng Zhang, and Fachao Jiang. "Questions and answers relating to lithium-ion battery safety issues". In: *Cell Reports Physical Science* 2.1 (2021) (cit. on p. 4).

[18] Jian Duan, Xuan Tang, Haifeng Dai, Ying Yang, Wangyan Wu, Xuezhe Wei, and Yunhui Huang. "Building safe lithium-ion batteries for electric vehicles: a review". In: *Electrochemical Energy Reviews* 3 (2020), pp. 1–42 (cit. on p. 4).

[19] Zeyu Chen, Rui Xiong, and Fengchun Sun. "Analysis and research status of battery safety accidents in electric vehicles". In: *Journal of mechanical engineering* 55.24 (2019), pp. 93–104 (cit. on p. 4).

[20] Xuning Feng, Siqi Zheng, Dongsheng Ren, Xiangming He, Li Wang, Hao Cui, Xiang Liu, Changyong Jin, Fangshu Zhang, Chengshan Xu, et al. "Investigating the thermal runaway mechanisms of lithium-ion batteries based on thermal analysis database". In: *Applied Energy* 246 (2019), pp. 53–64 (cit. on p. 4).

[21] Stefano Castegnaro. "Aerodynamic design of low-speed axial-flow fans: a historical overview". In: *Designs* 2.3 (2018), p. 20 (cit. on p. 4).

[22] B.E. S. Larry Dixon and C. Hall. *Fluid Mechanics and Thermodynamics of Turbomachinery*. Elsevier Science, 2013. ISBN: 9780124159549 (cit. on pp. 6, 7, 13, 16, 20).

[23] Xia Hua, Alan Thomas, and Kurt Shultis. "Recent progress in battery electric vehicle noise, vibration, and harshness". In: *Science Progress* 104.1 (2021). PMID: 33787408, p. 00368504211005224. DOI: 10.1177/00368504211005224. eprint: https://doi.org/10.1177/00368504211005224 (cit. on p. 6).

[24] Min-Jun Park and Duck-Joo Lee. "Sources of broadband noise of an automotive cooling fan". In: *Applied Acoustics* 118 (2017), pp. 66–75. ISSN: 0003-682X. DOI: https://doi.org/10.1016/j.apacoust.2016.10.007 (cit. on p. 6).

[25] LJ Leggat and TE Siddon. "Experimental study of the aeroacoustic mechanism of rotor–vortex interactions". In: *The Journal of the Acoustical Society of America* 64.4 (1978), pp. 1070–1077 (cit. on pp. 6, 59).

[26] Hiroshi Kobayashi and John F Groeneweg. "Effects of inflow distortion profiles on fan tone noise". In: *AIAA Journal* 18.8 (1980), pp. 899–906 (cit. on pp. 6, 59).

[27] Sharanya J Majumdar and Nigel Peake. "Noise generation by the interaction between ingested turbulence and a rotating fan". In: *Journal of Fluid Mechanics* 359 (1998), pp. 181–216 (cit. on pp. 6, 59).

[28] J Xie, Q Zhou, and Philip F Joseph. "Tone noise prediction of a propeller operating in nonuniform flows". In: *AIAA journal* 49.1 (2011), pp. 111–118 (cit. on pp. 6, 59).

[29] Till Heinemann, Sven Münsterjohann, Florian Zenger, and Stefan Becker. "Cross wind influence on noise emission and computed vibrational noise of an axial fan". In: *Turbo Expo: Power for Land, Sea, and Air*. Vol. 56628. American Society of Mechanical Engineers. 2015, V001T09A004 (cit. on pp. 6, 59).

[30] Martin Doherty and Howoong Namgoong. "Impact of turbofan intake distortion on fan noise propagation and generation". In: *22nd AIAA/CEAS Aeroacoustics Conference*. 2016, p. 2841 (cit. on pp. 6, 59).

[31] CL Morfey. "Rotating blades and aerodynamic sound". In: *Journal of Sound and Vibration* 28.3 (1973), pp. 587–617 (cit. on pp. 6, 59).

[32] BD Mugridge. "Axial flow fan noise caused by inlet flow distortion". In: *Journal of Sound and Vibration* 40.4 (1975), pp. 497–512 (cit. on pp. 6, 59).

[33] Th H Carolus and M Stremel. "Blade surface pressure fluctuations and acoustic radiation from an axial fan rotor due to turbulent inflow". In: *Acta Acustica united with ACUSTICA* 88.4 (2002), pp. 472–482 (cit. on pp. 6, 59).

[34] John P Wojno, Thomas J Mueller, and William K Blake. "Turbulence ingestion noise, Part 2: Rotor aeroacoustic response to grid-generated turbulence". In: *AIAA journal* 40.1 (2002), pp. 26–32 (cit. on pp. 6, 59).

[35] Alain Guedel. "Prediction of the Noise Installation Effect Induced by a Bend at the Inlet of an Axial Flow Fan." In: *Noise control engineering journal* 54.1 (2006) (cit. on pp. 6, 59).

[36] David B Stephens and Scott C Morris. "Sound generation by a rotor interacting with a casing turbulent boundary layer". In: *AIAA journal* 47.11 (2009), pp. 2698–2708 (cit. on pp. 6, 59).

[37] Rosalyn AV Robison and Nigel Peake. "Noise generation by turbulence–propeller interaction in asymmetric flow". In: *Journal of fluid mechanics* 758 (2014), pp. 121–149 (cit. on pp. 6, 59).

[38] T. Carolus. *Fans: Aerodynamic Design, Noise Reduction, Optimization*. Springer: Berlin/Heidelberg, Germany, 2022. ISBN: 978-3-658-37958-2 (cit. on pp. 7, 11, 13–18, 26–28, 33, 43, 59).

[39] Yonggang Gou, Xiuzhi Shi, Jian Zhou, Xianyang Qiu, and Xin Chen. "Characterization and effects of the shock losses in a parallel fan station in the underground mine". In: *Energies* 10.6 (2017), p. 785 (cit. on pp. 7, 8).

[40] Juan P Hurtado and EI Acuña. "CFD analysis of 58 Adit main fans parallel installation for the 2015–2019 underground developments of the new level mine project". In: *Applied Thermal Engineering* 90 (2015), pp. 1109–1118 (cit. on pp. 7, 8).

[41] Sandra Velarde Suárez, F Israel Guerras Colón, José González, Katia M Argüelles Díaz, Jesús M Fernández Oro, Carlos Santolaria-Morros, and Juan Bernal-Cantón. "Evaluation of Interaction and Blockage Effects for Multi-fan Units used in Public Transport HVAC Systems". In: *International Journal of Ventilation* 13.4 (2015), pp. 339–350 (cit. on pp. 7, 8).

[42] Florian Zenger, Clemens Junger, Manfred Kaltenbacher, and Stefan Becker. *A benchmark case for aerodynamics and aeroacoustics of a low pressure axial fan*. Tech. rep. SAE Technical Paper, 2016 (cit. on pp. 8, 13, 20, 51, 52, 54, 56, 57, 59).

[43] Florian J. Krömer. "Sound emission of low-pressure axial fans under distorted inflow conditions". doctoralthesis. FAU University Press, 2018, XVIII, 253 S. DOI: 10.25593/978-3-96147-089-1 (cit. on pp. 8, 21, 28, 35, 36, 51, 52, 54, 56, 57, 59).

[44] Thomas H Carolus and Ralf Starzmann. "An aerodynamic design methodology for low pressure axial fans with integrated airfoil polar prediction". In: *Turbo Expo: Power for Land, Sea, and Air*. Vol. 54648. 2011, pp. 335–342 (cit. on pp. 11, 26, 59).

[45] *Industrial fans - Performance testing using standardized airways*. Standard. International Organization for Standardization, 2007 (cit. on p. 11).

[46] Peter F. Pelz and Stefan S. Stonjek. "The Influence of Reynolds Number and Roughness on the Efficiency of Axial and Centrifugal Fans—A Physically Based Scaling Method". In: *Journal of Engineering for Gas Turbines and Power* 135.5 (Apr. 2013). 052601. ISSN: 0742-4795. DOI: 10.1115/1.4022991. eprint: https://asmedigitalcollection.asme.org/gasturbinespower/article-pdf/135/5/052601/6157539/gtp_135_5_052601.pdf (cit. on p. 13).

[47] Jie Wang and Niels P. Kruyt. "Computational Fluid Dynamics Simulations of Aerodynamic Performance of Low-Pressure Axial Fans With Small Hub-to-Tip Diameter Ratio". In: *Journal of Fluids Engineering* 142.9 (May 2020). 091202. ISSN: 0098-2202. DOI: 10.1115/1.4047120. eprint: https://asmedigitalcoll\-ection.asme.org/fluidsengineering/article-pdf/142/9/091202/6537190/fe_142_09_091202.pdf (cit. on pp. 13, 20, 26).

[48] Jie Wang and Niels P Kruyt. "Effects of sweep, dihedral and skew on aerodynamic performance of low-pressure axial fans with small hub-to-tip diameter ratio". In: *Journal of Fluids Engineering* 144.1 (2022) (cit. on pp. 13, 20, 26).

[49] Massimo Masi, Manuel Piva, and Andrea Lazzaretto. "Design guidelines to increase the performance of a rotor-only axial fan with constant-swirl blading". In: *Turbo Expo: Power for Land, Sea, and Air*. Vol. 45578. American Society of Mechanical Engineers. 2014, V01AT10A033 (cit. on pp. 13, 20, 26).

[50] J Vad, A. R A. Kwedikha, Cs Horváth, M Balczó, M. M. Lohász, and T Régert. "Aerodynamic effects of forward blade skew in axial flow rotors of controlled vortex design". In: *Proceedings of the Institution of Mechanical Engineers, Part A: Journal of Power and Energy* 221.7 (2007), pp. 1011–1023. DOI: 10.1243/09576509JPE420. eprint: https://doi.org/10.1243/09576509JPE420 (cit. on pp. 13, 20).

[51] M. G. Beiler and T. H. Carolus. "Computation and Measurement of the Flow in Axial Flow Fans With Skewed Blades". In: *Journal of Turbomachinery* 121.1 (Jan. 1999), pp. 59–66. ISSN: 0889-504X. DOI: 10.1115/1.2841234. eprint: https://asmedigitalcollection.asme.org/turbomachinery/article-pdf/121/1/59/5725321/59_1.pdf (cit. on pp. 13, 20).

[52] Nicola Aldi, Nicola Casari, Michele Pinelli, and Alessio Suman. "A statistical survey on the actual state-of-the-art performance of radial flow fans based on market data". In: *Proceedings of FAN 2018 Conference*. 2018, pp. 18–20 (cit. on p. 13).

[53] Isaak E Idelchik. "Handbook of hydraulic resistance". In: *Washington* (1986) (cit. on p. 15).

[54] Otto Cordier. "Ähnlichkeitsbedingungen für Strömungsmaschinen". In: *BWK Bd* 6.10 (1953) (cit. on pp. 16, 17).

[55] János Vad and Ferenc Bencze. "Three-dimensional flow in axial flow fans of non-free vortex design". In: *International Journal of Heat and Fluid Flow* 19.6 (1998), pp. 601–607. ISSN: 0142-727X. DOI: https://doi.org/10.1016/S0142-727X(98)10004-8 (cit. on p. 20).

[56] Simon J. Gallimore, John J. Bolger, Nicholas A. Cumpsty, Mark J. Taylor, Peter I. Wright, and James M. M. Place. "The Use of Sweep and Dihedral in Multistage Axial Flow Compressor Blading—Part I: University Research and Methods Development ". In: *Journal of Turbomachinery* 124.4 (Nov. 2002), pp. 521–532. ISSN: 0889-504X. DOI: 10.1115/1.1507333. eprint: https://asmedigitalcollection.asme.org/turbomachinery/article-pdf/124/4/521/5528949/521_1.pdf (cit. on p. 20).

[57] A Corsini and F Rispoli. "Using sweep to extend the stall-free operational range in axial fan rotors". In: *Proceedings of the Institution of Mechanical Engineers, Part A: Journal of Power and Energy* 218.3 (2004), pp. 129–139. DOI: 10.1243/095765004323049869. eprint: https://doi.org/10.1243/095765004323049869 (cit. on p. 20).

[58] Thomas Carolus and Konrad Bamberger. "Axial Impeller-Only Fans with Optimal Hub-to-Tip Ratio and Blades Adapted for Minimum Exit Loss". In: *International Journal of Turbomachinery, Propulsion and Power* 8.1 (2023). ISSN: 2504-186X (cit. on p. 26).

[59] Ira H Abbott and Albert E Von Doenhoff. *Theory of wing sections: including a summary of airfoil data*. Courier Corporation, 2012 (cit. on p. 27).

[60] Mark Drela. "XFOIL: An analysis and design system for low Reynolds number airfoils". In: *Low Reynolds Number Aerodynamics: Proceedings of the Conference Notre Dame, Indiana, USA, 5–7 June 1989*. Springer. 1989, pp. 1–12 (cit. on pp. 27, 44).

[61] William K Blake. *Mechanics of flow-induced sound and vibration, Volume 2: Complex flow-structure interactions*. Academic press, 2017 (cit. on pp. 32, 33).

[62] Wolfgang Neise and Ulf Michel. "Aerodynamic noise of turbomachines". In: *Deutsche Forschungsanstalt für Luft-und Raumfahrt, eV, DLR, Institut für Strömungsmechanik, Abt. Turbulenzforschung, Berlin* 5 (1994) (cit. on pp. 32, 34, 35).

[63] SE Wright. "The acoustic spectrum of axial flow machines". In: *Journal of Sound and Vibration* 45.2 (1976), pp. 165–223 (cit. on pp. 32, 33, 35, 36).

[64] Thomas F Brooks, D Stuart Pope, and Michael A Marcolini. *Airfoil self-noise and prediction*. Tech. rep. 1989 (cit. on p. 32).

[65] RE Longhouse. "Control of tip-vortex noise of axial flow fans by rotating shrouds". In: *Journal of sound and vibration* 58.2 (1978), pp. 201–214 (cit. on p. 33).

[66] T Fukano, Y Takamatsu, and Y Kodama. "The effects of tip clearance on the noise of low pressure axial and mixed flow fans". In: *Journal of sound and vibration* 105.2 (1986), pp. 291–308 (cit. on p. 33).

[67] Choon-Man Jang, Tohru Fukano, and Masato Furukawa. "Effects of the tip clearance on vortical flow and its relation to noise in an axial flow fan". In: *JSME International Journal Series B Fluids and Thermal Engineering* 46.3 (2003), pp. 356–365 (cit. on p. 33).

[68] T Fukano and C-M Jang. "Tip clearance noise of axial flow fans operating at design and off-design condition". In: *Journal of sound and vibration* 275.3-5 (2004), pp. 1027–1050 (cit. on p. 33).

[69] Mirko Cudina. "Noise generated by a vane-axial fan with inlet guide vanes". In: *Noise Control Engineering Journal* 39.1 (1992), pp. 21–30 (cit. on p. 33).

[70] RK Amiet. "Thickness noise of a propeller and its relation to blade sweep". In: *Journal of Fluid Mechanics* 192 (1988), pp. 535–560 (cit. on p. 34).

[71] L Gutin. "On the sound field of a rotating propeller". In: *Physikalische Zeitschrit der Sowjetinion: Physical magazine of the Soviet Union volume 9 number 1* 9.NACA-TM-1195 (1948) (cit. on p. 34).

[72] Frank Kameier and Wolfgang Neise. "Experimental study of tip clearance losses and noise in axial turbomachines and their reduction". In: (1997) (cit. on p. 34).

[73] Ronald Mailach, Ingolf Lehmann, and Konrad Vogeler. "Rotating instabilities in an axial compressor originating from the fluctuating blade tip vortex". In: *J. Turbomach.* 123.3 (2001), pp. 453–460 (cit. on p. 34).

[74] Tao Zhu, Dominic Lallier-Daniels, Marlène Sanjosé, Stéphane Moreau, and Thomas Carolus. "Rotating coherent flow structures as a source for narrowband tip clearance noise from axial fans". In: *Journal of Sound and Vibration* 417 (2018), pp. 198–215 (cit. on p. 34).

[75] Stéphan Magne, Stéphane Moreau, and Alain Berry. "Subharmonic tonal noise from backflow vortices radiated by a low-speed ring fan in uniform inlet flow". In: *The Journal of the Acoustical Society of America* 137.1 (2015), pp. 228–237 (cit. on p. 34).

[76] A. H. Stenning. "Rotating Stall and Surge". In: *Journal of Fluids Engineering* 102.1 (Mar. 1980), pp. 14–20. ISSN: 0098-2202. DOI: 10.1115/1.3240618. eprint: https://asmedigitalcollection.asme.org/fluidsengineering/article-pdf/102/1/14/5898556/14_1.pdf (cit. on p. 35).

[77] CL Morfey. "The acoustics of axial flow machines". In: *Journal of Sound and Vibration* 22.4 (1972), pp. 445–466 (cit. on p. 35).

[78] R Minniti III, W Blake, and T Mueller. "Determination of inflow distortions by interpreting aeroacoustic response of a propeller fan". In: *4th AIAA/CEAS Aeroacoustics Conference*. 1998, p. 2286 (cit. on p. 35).

[79] Hauke Reese, Thomas Carolus, and Chisachi Kato. "Numerical prediction of the aeroacoustic sound sources in a low pressure axial fan with inflow distortion". In: *Fan noise* 9 (2007), 1–12P (cit. on p. 35).

[80] M Shur, M Strelets, A Travin, J Christophe, K Kucukcoskun, CF Schram, S Sack, and M Åbom. "Effect of inlet distortions on ducted fan noise, 22nd AIAA". In: *CEAS Aeroacoustics Conference*. 2016, p. 2819 (cit. on p. 35).

[81] J.E. Ffowcs Williams and D.L. Hawkings. "Sound Generated by Turbulence and Surfaces in Arbitrary Motion". In: *Philosophical Transactions of the Royal Society* A264.1151 (1969), pp. 321–342 (cit. on p. 38).

[82] F Farassat and M.K. Myers. "Extension of Kirchhoff's Formula to Radiation from Moving Surfaces". In: *Journal of Sound and Vibration* 123.3 (1999), pp. 451–461 (cit. on p. 38).

[83] P De Haller. “Das verhalten von tragflügelgittern in axialverdichtern und im windkanal”. In: *Brennstoff-Wärme-Kraft (BWK)* 5.333 (1953), p. 24 (cit. on p. 46).

[84] Heinz Marcinowski. “" Optimalprobleme bei Axialventilatoren”. PhD thesis. Technischen Hochsehule, 1956 (cit. on p. 46).

[85] Frank Schiller. “Theoretical and experimental studies to determine the load limit for highly loaded axial fans”. PhD thesis. Technical University of Braunschweig, 1984 (cit. on p. 46).